

MEASUREMENTS OF THE SELF-ASSEMBLY KINETICS OF INDIVIDUAL VIRAL CAPSIDS AROUND THEIR RNA GENOME

REES F. GARMANN^{1,†}, AARON M. GOLDFAIN^{1,†}, AND VINOTHAN N.
MANOHARAN^{1,2}

5

The formation of a viral capsid—the highly-ordered protein shell that surrounds the genome of a virus—is the canonical example of self-assembly¹. The capsids of many positive-sense RNA viruses spontaneously assemble from *in vitro* mixtures of the coat protein and RNA². The high yield of proper capsids that assemble is remarkable, given their structural complexity: 180 identical proteins must arrange into three distinct local configurations to form an icosahedral capsid with a triangulation number of 3 ($T = 3$)¹. Despite a wealth of data from structural studies^{3–5} and simulations^{6–10}, even the most fundamental questions about how these structures assemble remain unresolved. Experiments have not determined whether the assembly pathway involves aggregation or nucleation, or how the RNA controls the process. Here we use interferometric scattering microscopy^{11,12} to directly observe the *in vitro* assembly kinetics of individual, unlabeled capsids of bacteriophage MS2. By measuring how many coat proteins bind to each of many individual MS2 RNA strands on time scales from 1 ms to 900 s, we find that the start of assembly is broadly distributed in time and is followed by a rapid increase in the number of bound proteins. These measurements provide strong evidence for a nucleation-and-growth pathway. We also find that malformed structures assemble when multiple nuclei appear on the same RNA before the first nucleus has finished growing. Our measurements reveal the complex assembly pathways for viral capsids around RNA in quantitative detail, including the nucleation threshold, nucleation time, growth time, and constraints on the critical nucleus size. These results may inform strategies for engineering synthetic capsids¹³ or for derailing the assembly of pathogenic viruses¹⁴.

¹HARVARD JOHN A. PAULSON SCHOOL OF ENGINEERING AND APPLIED SCIENCES, CAMBRIDGE, MA 02138 USA

²DEPARTMENT OF PHYSICS, HARVARD UNIVERSITY, CAMBRIDGE, MA 02138 USA

[†]EQUAL CONTRIBUTION

E-mail address: vnm@seas.harvard.edu.

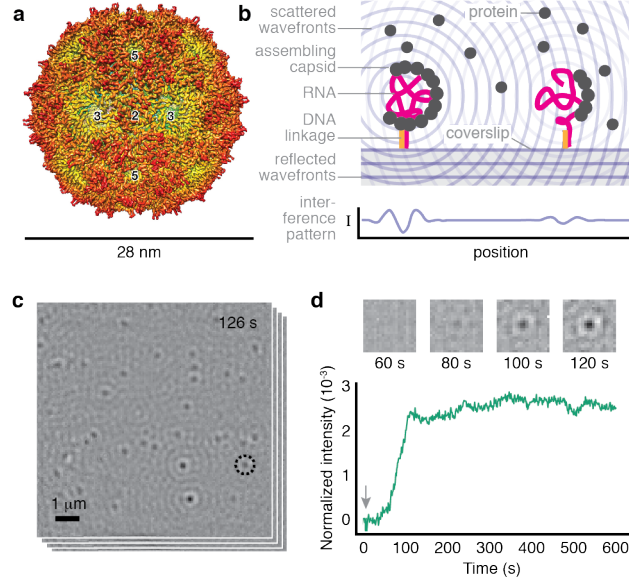


FIGURE 1. Overview of the system and measurement.

(a) A structural model of the MS2 capsid from cryo-electron microscopy data (reproduced from Ref. 5) reveals its icosahedral structure with 2-, 3-, and 5-fold symmetry axes. (b) We inject a solution of MS2 coat-protein dimers over a coverslip on which MS2 RNA strands are tethered by DNA linkages¹⁵. As the proteins bind to the RNA, the resulting particles scatter light. Owing to destructive interference between the scattered light and a reference beam, the particles appear as dark, diffraction-limited spots. (c) We monitor many individual assembling particles in parallel. A typical image, taken 126 s after adding 2 μM dimers and representing an average of 1,000 frames taken at 1,000 frames/s, shows multiple spots. (d) The intensity of a spot as a function of time reveals the assembly kinetics of an individual particle. Top: time-series of images for the circled spot in (c). Bottom: kinetic trace for the same spot using a 1,000-frame average of data taken at 1,000 frames/s. The arrow indicates when we inject the coat protein.

We work with MS2 (Fig. 1a) because it is a non-trivial model system for understanding capsid assembly: Complete 28-nm capsids can be assembled *in vitro* from the coat proteins and RNA¹⁶; the assembled capsids have $T = 3$ (90 coat-protein dimers)¹⁷, such that they must compete with many possible malformed structures; and the RNA is suspected to play an important role in the assembly process^{18–22}. Experiments probing assembly in bulk solution

have shown that specific RNA sequences might initiate assembly by binding the first few coat proteins²². But because such measurements probe an ensemble of particles in possibly different stages of assembly, they can obscure important features of the assembly pathway. The equally important question of how that pathway can be derailed—leading to the often-overlooked minority of malformed structures observed in bulk assembly of bacteriophages¹⁸ and other viruses^{23–25}—also remains unresolved.

Our interferometric scattering experiments address these questions because they probe the assembly of individual capsids (Fig. 1b–d). As described in Methods, each assembling particle produces a diffraction-limited spot in the field of view. Because continuous background correction in our measurement renders the RNA invisible, the final signal depends only on the number of proteins in the assembling particle. Thus, the time trace of the intensity for each spot gives a direct measure of the assembly kinetics of an individual particle.

We must measure the intensity of each spot with both high sensitivity and high dynamic range, because the capsids scatter weakly, and estimates of the assembly times range from seconds²⁰ to hours^{20,22}. Our apparatus (Extended Data Fig. 1) addresses both of these challenges. Because the scattering is elastic, we can use high illumination intensities with minimal risk of photodamage, enabling temporal resolutions of 1 ms. To simultaneously achieve durations of 900 s, we actively stabilize the microscope in all three dimensions, ensuring that the signal from the assembling capsid is larger than the noise due to drift. The sensitivity is then limited by shot noise. With a 1-s moving average, as shown in Fig. 1d, the peak-to-peak fluctuations from shot noise correspond to the intensity of six coat-protein dimers.

In a single experiment, we measure kinetic traces for many assembling particles in parallel, and we characterize the shape of each trace as well as variations among traces. When we inject 2 μ M coat-protein dimers, we find that most traces have an initial plateau at a low intensity followed by a rapid rise and a second plateau at higher intensity (Fig. 2a and Extended Data Fig. 2). A few traces show intermediate plateaus. Most (40 out of 56) plateau at an intensity consistent with that of a full, wild-type capsid (Extended Data Fig. 3), 7 at a slightly lower intensity, and 9 at a significantly higher intensity. No such traces are observed when RNA is not tethered to the coverslip (Supplementary Information). Furthermore, negatively stained transmission electron microscopy (TEM) images reveal that most of the structures assembled in control experiments are proper capsids, with a few partial capsids and larger structures visible (Fig. 2b and Extended Data Fig. 4). We therefore infer that capsids can indeed assemble around tethered RNA strands, and that traces that reach intensities similar to those of wild-type capsids represent the formation of complete or nearly-complete capsids.

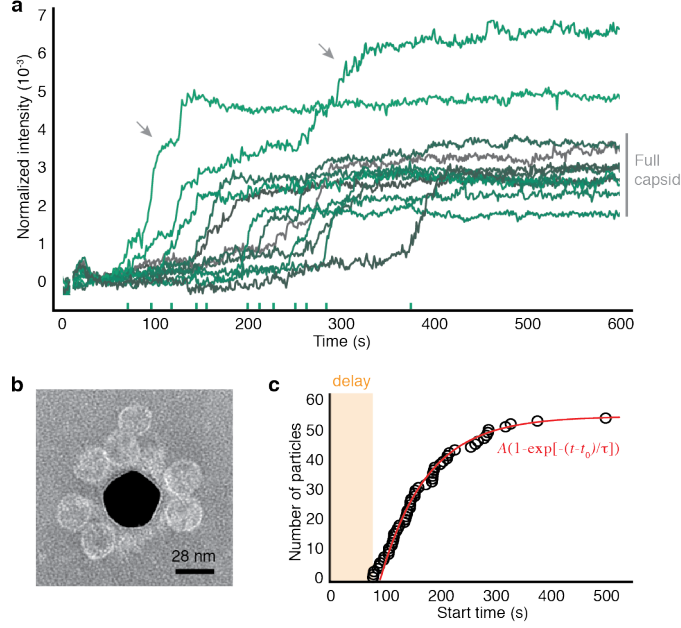


FIGURE 2. Assembly of 2 μ M coat-protein dimers around surface-tethered RNA strands. (a) Kinetic traces for 12 randomly chosen particles. Ticks on the x-axis show the start times. Grey bar indicates the intensity range corresponding to wild-type capsids. Arrows point to two traces corresponding to overgrown particles. (b) A negatively stained TEM image of particles assembled around RNA strands tethered to a gold nanoparticle (dark region at center). We use a nanoparticle as the substrate because TEM cannot image through a coverslip. (c) The cumulative distribution of start times in the traces is well fit by an exponential function with $A = 56.62 \pm 0.02$, $t_0 = 91.8 \pm 0.2$ s, and $\tau = 84.3 \pm 0.2$ s. Uncertainties in the time measurements are smaller than the diameter of the circles.

With this understanding, we examine what the traces reveal about the assembly pathway. A key observation is that assembly is not synchronous: 85
the ‘start time’, the time at which the intensity rapidly increases, varies from particle to particle (Fig. 2a). We find that the cumulative distribution of start times t is fit well by an exponential function $A(1 - \exp[-(t - t_0)/\tau])$ (Fig. 2c), where A is the plateau value, t_0 is the delay before the start time of the first particle, and τ is the characteristic time (see Methods and Extended 90
Data Fig. 5.)

The delay likely results from the combination of diffusion and a concentration threshold for assembly. We know such a threshold exists because we

see no assembly when we inject 1 μM coat-protein dimers (Extended Data Fig. 6). Because the threshold is between 1 and 2 μM coat-protein dimers, we expect the delay to be of the order of the characteristic time for protein to diffuse from the 2 μM injected fluid to the surface. Indeed, that time scale is 30–55 s (Supplementary Information), and the observed delay time is 92 s.

The distribution of start times, however, does not appear to result from diffusion. The distribution is broad, with the largest start time (500 s) an order of magnitude larger than the delay time. The distribution could result from diffusion-limited growth only if the protein concentration around each RNA were to vary across the 10- μm field of view. But the time for a dimer to diffuse 10 μm is only 1 s, much shorter than the median start time. Furthermore, we estimate that about 1,000 coat-protein dimers are within 1 μm of each RNA after the initial delay. At this concentration, the pool of coat proteins is not significantly depleted by assembly, and fluctuations in concentration are negligible. We conclude that the observed kinetic traces do not result from variations in protein concentration.

Taken together, these findings rule out a diffusion-limited aggregation pathway and point strongly to nucleation and growth. The exponential shape of the cumulative distribution of start times suggests a well-defined free-energy barrier to nucleation with a nucleation time of τ . Although nucleation models have been used to describe the bulk assembly kinetics of empty capsids^{26–28}, and computer simulations have explored nucleated pathways for capsid assembly around RNA^{8–10}, direct experimental evidence for nucleation has remained elusive. The evidence that we present—the distribution of start times—cannot easily be extracted from bulk experiments²², which average over an ensemble of particles, or from structural experiments²⁹, which have coarse temporal resolution.

Fluctuations in the intensity reveal further information about the nucleation event. Before the start time, the fluctuations are consistent with those expected from shot noise, which, as noted above, corresponds to six dimers at 1-s averaging. This measurement indirectly constrains the critical nucleus size: we can infer that sub-critical nuclei smaller than six dimers do not survive for longer than 1 s.

Additional nucleation events may be responsible for assembly going awry in some of the capsids. Most of the traces with final plateau intensities higher than that of a full capsid also show intermediate plateaus at intensities consistent with that of a full capsid (Fig. 2a). Such traces suggest that the particle undergoes a second nucleation event after the first capsid is nearly complete.

To test this hypothesis, we measure the kinetics at different concentrations of protein (Fig. 3a, and Extended Data Figs. 7 and 8). We find that the nucleation time decreases with increasing protein concentration, from about 160 s at 1.5 μM dimers to about 11 s at 4 μM (Fig. 3b). This decrease is accompanied by an increase in the fraction of overgrown particles, from 5%

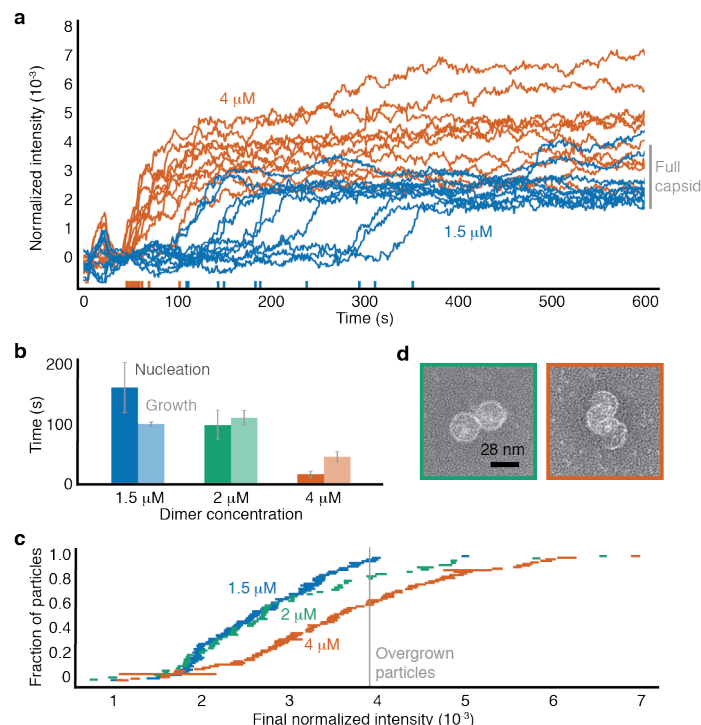


FIGURE 3. Assembly kinetics at different protein concentrations. (a) Kinetic traces for 10 randomly chosen particles at 1.5 μM and 4 μM coat-protein dimers. (b) Measured nucleation times and median growth times. Error bars represent the standard deviation from three experiments. (c) Cumulative distributions of the final intensities show that the fraction of overgrown particles increases with protein concentration. The length of each horizontal bar is the standard deviation calculated from the last 50 s of each trace. (d) TEM images of overgrown particles around untethered RNA. Left: an attached pair of nearly complete capsids at 2 μM protein. Right: connected partial capsids at 4 μM protein.

at 1.5 μM dimers to over 40% at 4 μM (Fig. 3c). TEM images of assembly reactions around untethered RNA (Extended Data Fig. 9) show overgrown particles with sizes corresponding to the final intensities seen in the kinetic traces. Many of the overgrown particles consist of bunches of partial or nearly-complete capsids (Fig. 3d).

The kinetic traces and images of the overgrown structures suggest a pathway involving more than one nucleation event. However, many of the traces at 4 μM coat-protein dimers do not show intermediate plateaus (Fig. 3a). To understand why, we measure how long it takes a particle to reach the intensity of a full capsid after it starts growing (see Methods). We find that

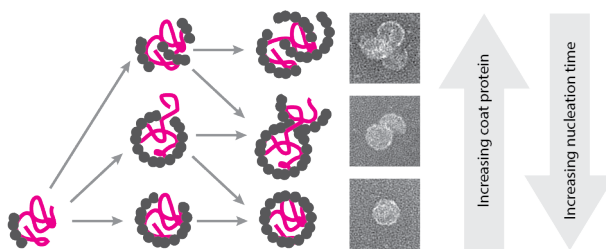


FIGURE 4. Cartoon of the inferred assembly pathways. First, a nucleus of coat proteins forms on the RNA. Bottom row: At low protein concentration, no additional nuclei form, and the nucleus grows into a proper capsid. Middle row: At higher concentrations, a second nucleus can form on an unpackaged part of the RNA, leading to a multiplet structure consisting of a nearly-complete capsid attached to a second partial or full capsid. Top row: At even higher concentrations, multiple nuclei can form and grow, leading to a monster structure consisting of many partial capsids. Example TEM images of the endpoints of each pathway are shown at right.

these ‘growth times’ decrease with increasing protein concentration, but less rapidly than do the nucleation times (Fig. 3b). When the nucleation time is smaller than the growth time, as it is in experiments with 4 μ M dimers, additional nuclei can form before the first has time to grow. Under such conditions, most of the kinetic traces should not—and indeed, do not—show intermediate plateaus.

Thus, the viral RNA creates a competition between nucleation and growth, as sketched in Fig. 4. Similar scenarios have been observed in computer simulations of capsid assembly on polymer scaffolds^{8,9}, and may explain the formation of the ‘monster’²³ and ‘multiplet’^{24,25} structures observed in experiments with other viruses. These structures are not observed in experiments on the assembly of empty capsids^{30,31}, confirming that the RNA plays a critical role in the assembly pathways.

Our individual-particle measurements also rule out some competing pathways. The assembly of proper capsids appears to follow a one-step nucleation pathway rather than a multi-step one³². Also, the formation of overgrown structures appears to result from multiple nucleation events rather than the ‘spiraling’ pathway^{6,7} observed in local rules-based simulations, or the ‘en-masse’ pathway^{8,9} observed in Brownian dynamics simulations. Because our measurements involve thermally annealed RNA (see Methods), they do not yet resolve whether the pathway is fine-tuned by local folding patterns in the viral RNA^{33,34}.

While our observations are specific to *in vitro* assembly, the observed threshold concentration for nucleation supplies a hypothesis for viral replication *in vivo*. Because viral RNA that is inside a capsid cannot be replicated or translated, a virus such as MS2 must delay encapsidation until its components have been produced in sufficient quantities. With a threshold for nucleation, assembly (and encapsidation) would take place only after there is enough viral RNA and coat protein to form many new virus particles. 175

Although we expect the assembly pathways to differ for different viruses and buffer conditions, our measurements of the nucleation time, threshold, growth time, and subcritical fluctuations in MS2 provide important constraints on models of assembly. As a result, the structures of the assembly intermediates and the critical nucleus, which have long eluded direct imaging methods, might now be inferred through quantitative comparisons of simulated^{8,9} and measured individual-particle kinetics. This approach might identify conditions for assembly of synthetic viruses¹³ and new targets for antiviral therapies that work by disrupting capsid assembly¹⁴. 180 185

METHODS

Interferometric scattering microscope. Our microscope is configured in wide-field mode and is similar to the setup described by Ortega-Arroyo and coworkers³⁵. A 450 nm, 100 mW, single-mode diode laser (PD-01251, Lasertack) illuminates the sample. The current driving the laser is modulated with a square wave at a frequency of 1 MHz to decrease the coherence of the laser and limit intensity variations in the background³⁶. The beam (shown in blue in Extended Data Fig. 1) is spatially filtered by a polarization-maintaining single-mode optical fiber (fiber 1; PM-S405-XP, Thorlabs). The filtered light is collected by a lens (lens 1; achromatic doublet, focal length = 25 mm, Thorlabs), reflected from a polarizing beamsplitter cube (CCM1-PBS251, Thorlabs), and focused onto the back aperture of the objective (100 \times oil-immersion, 1.45 NA Plan Apo λ , Nikon) to produce collimated illumination in the imaging chamber. The light that is backscattered from the sample and light that is reflected from the water-coverslip interface are collected by the objective and imaged onto camera 1 (MV1-D1024E-160-CL, Photon Focus) by the tube lens (achromatic doublet, focal length = 300 mm, Thorlabs). We use achromatic half and quarter-wave plates (AHWP3 and AQWP3, Bolder Vision Optik) with the polarizing beamsplitter to make an optical isolator that minimizes the intensity lost at the beamsplitter. The total magnification is 150 \times , such that each pixel on the camera views a field of 70 nm. All images are recorded with a bit depth of 12.

The illumination intensity, set to approximately 3 kW/cm² when we record data at 1,000 Hz and 0.3 kW/cm² at 100 Hz, is similar to that typically used in single-molecule fluorescence experiments³⁷. To minimize any possible radiation damage, we use an exposure time that is almost equal to the total time between frames, and we dim the imaging beam with absorptive filters so that the camera pixels are nearly saturated. The total field of view is 140 pixels \times 140 pixels (9.8 μ m \times 9.8 μ m) at 1,000 Hz and 200 pixels \times 200 pixels (14 μ m \times 14 μ m) at 100 Hz.

We use short-wavelength light ($\lambda = 450$ nm) because the intensity of the image scales with λ^{-2} . While shorter wavelength lasers are available, we find that they can damage both the sample and optical components when used at high intensities. Control experiments at different illumination intensities are described below and in Supplementary Information, which also contains additional notes on the configuration of the microscope.

The intensity of each diffraction-limited spot is approximately linearly proportional to the number of proteins bound to the RNA strand. The intensity of a spot is $I = I_r + I_s + 2\sqrt{I_r I_s} \cos \phi_{rs}$, where I_r is the intensity of the reflected wave, I_s the intensity of the scattered wave, and ϕ_{rs} the phase difference between the two. The term I_s can be neglected since the scattered light is dim compared to the reflected light, so the normalized intensity $I_{\text{norm}} = I/I_r - 1$ is proportional to the total polarizability of the assembling particle¹², which is approximately the sum of a protein component and an

RNA component. Because the RNA component is static, it is part of the background, which is subtracted. As a result, the normalized intensity is linearly proportional to the number of proteins in the assembling particle.

Active stabilization. The position of the coverslip relative to the objective is actively stabilized to a few nanometers in all three dimensions. Each dimension is controlled separately through a proportional control loop on the PC. During each iteration of the loop, the position of the coverslip is measured, and the voltage driving the piezoelectric actuators is modified to keep the coverslip in its original position.

The height of the coverslip above the objective is measured by tracking the position of a laser (red in Extended Data Fig. 1) that is totally internally reflected by the coverslip-water interface, as described by Ortega-Arroyo and coworkers³⁵. We use a 785-nm, 90 mW, single-mode diode laser (L785P090, Thorlabs) that is coupled through a single-mode fiber (fiber 2; S630-HP, Thorlabs). The laser is driven with a constant current (27 mA) that is well below threshold (35 mA), which we find improves the intensity stability of the laser. After exiting the optical fiber, the beam is collected by lens 2 (plano-convex, focal length = 20 mm, Thorlabs), reflects from a dichroic mirror (700-nm short-pass, Edmund Optics), and is focused onto the back aperture of the objective. We align the beam so that after exiting the objective, it totally internally reflects from the coverslip-water interface and re-enters the objective. The total power incident on the coverslip is less than 1 μ W. The return beam reflects from the coverslip and then from a D-shaped mirror (Thorlabs) and is detected with camera 2 (DCC1545M, Thorlabs). A long-pass filter (700-nm, Thorlabs, not shown in Extended Data Fig. 1) attenuates any light from the imaging beam that is also incident on camera 2. When the height of the coverslip changes, the return beam is displaced laterally across camera 2, resulting in a change in the measured center-of-brightness. Under active stabilization, any changes in the center-of-brightness are measured and corrected every 30 ms.

The in-plane position of the coverslip is measured by tracking a 30-nm gold particle that is adsorbed to the coverslip surface (see next subsection for details of how we prepare the coverslips). Before each experiment, we find one of the adsorbed gold particles by looking for spots that have a normalized intensity of approximately 0.2. We then move the coverslip so that the spot is near the edge of the field of view. Using a 16×16 -pixel region of the field of view, we record a static background image of the coverslip with no particles present and then move the gold particle into the center of this small field of view. Before tracking the position of the gold particle, we process its image in the small field of view by subtracting off the static background, applying a bandpass filter (passing features of size 1 to 7 pixels) to smooth the image, and taking the time-median of 33 images of the particle (recorded at 33 Hz) to reduce shot noise. We then use the program Trackpy³⁸ to locate the position of the particle. We use this position for the active stabilization

loop, which runs once per second. The in-plane control loop frequency (1 275 Hz) is lower than that of the out-of-plane control loop (33 Hz) because of the time required to collect the median image of the particle.

The active stabilization loops are implemented in a Python script (<http://github.com/manoharan-lab/camera-controller>). The same script includes a real-time image processing routine that allows us to see growing 280 MS2 particles while collecting data.

Coverslip and gold nanoparticle functionalization. We adapt the protocols described by Joo and Ha³⁹ to coat glass coverslips with a layer of PEG molecules, about 1% of which are functionalized with short DNA oligonucleotides. We find that many brands of #2 coverslips are unsuitable for 285 assembly measurements because they have imperfections that scatter too much light. We use only #2 thickness, 24 mm \times 60 mm rectangular glass microscope coverslips from Globe Scientific, Inc. Details of how we functionalize the coverslips and decorate them with 30-nm gold particles are in Supplementary Information. 290

Flow cell design and construction. We build chips that each contain 10 separate flow cells above a single coverslip. Each chip consists of two sheets of cut, clear acrylic that are sealed together and to the coverslip with melted Parafilm (Bemis). Each flow cell has an imaging chamber that is 295 used for the assembly experiments, an inlet cup to hold fluid before it is introduced into the imaging chamber of the flow cell, a short inlet chamber to connect the inlet cup to the imaging chamber, and an outlet chamber. We use acrylic, a hard plastic, because we find that soft materials such as polydimethylsiloxane lead to more warping of the coverslip during injection of the protein. A detailed description of the flow cells and their construction 300 is given in Supplementary Information.

Growth of MS2 and purification of its coat protein and RNA. We grow wild-type MS2 by infecting liquid cultures of *E. coli* strain C3000 (a gift from Peter Stockley at the University of Leeds) and purifying the progeny viruses following the protocols of Strauss and Sinsheimer⁴⁰. We purify coat 305 protein from the virus particles following the cold acetic acid method described by Sugiyama, Hebert, and Hartmann¹⁶. We purify RNA from freshly grown MS2 virions using an RNA extraction kit (RNeasy, Qiagen). Details about how we assess the purity of these materials are described in Supplementary Information. 310

We store the purified virus particles at 4 °C and discard them after about 1 month. We store the protein at 4 °C and discard it after 1 week. We store the RNA at -80 °C and discard it after about 1 year.

Surface-immobilization of MS2 RNA by DNA linkages. To immobilize MS2 RNA at the coverslip surface, we first hybridize the 5'-end of the 315 RNA to a 60-base-long linker oligo (Integrated DNA Technologies). The 40 bases at the 5'-end of the linker are complementary to the 40 bases at the

5'-end of the RNA, and the remaining 20 bases are complementary to the sequence of the surface oligo (Extended Data Fig. 1). To anneal the linker to the MS2 RNA, we add a 10-fold molar excess of the linker oligo to 500 nM MS2 RNA in hybridization buffer (50 mM Tris-HCl, pH 7.0; 200 mM NaCl, 1 mM EDTA), heat the mixture to 90 °C for 1 s, and then cool it to 4 °C at a rate of -1 °C/s. Excess linker is removed with a 100-kDa-MWCO centrifugal filter unit (EMD Millipore) at 14,000 g. The 60-base-long oligonucleotides do not pass through the filter; instead, they stick to the membrane. We confirm RNA-DNA binding by native 1% agarose gel electrophoresis (Supplementary Information). We confirm that the RNA-DNA constructs specifically bind our DNA-functionalized coverslips by interferometric scattering microscopy (Supplementary Information). The sequence of the linker is 5'-CGACAGGAAGTTGAGCAGGACCCCGAAAGGGTCCCAACCAACCAACCAACCAACC-3'

Calibration experiment. We measure the intensities of MS2 RNA and wild-type MS2 virus particles (Extended Data Fig. 3) by imaging the particles as they adsorb to an APTES-functionalized coverslip. For these experiments we do not use a flow cell. Instead, we use a 'lean-to' sample chamber⁴¹ made of 1-mm-thick glass slides (Micro Slides, Corning) that are cut, cleaned by pyrolysis (PYRO-CLEAN, Tempyrox Co.), and sealed in place with vacuum grease (High vacuum grease, Dow Corning). To perform the calibration experiment, we first fill the sample chamber with TNE buffer (50 mM Tris-HCl, pH 7.5; 100 mM NaCl; 1 mM EDTA) and focus the microscope onto the coverslip. We then exchange the buffer in the sample chamber with a solution containing both MS2 RNA and wild-type MS2 virus particles at a concentration of 0.1 nM each in TNE buffer. We record movies (100 Hz) of these particles nonspecifically adsorbing to the coverslip.

We see two well-separated populations in the distribution of intensities of the particles that bind (Extended Data Fig. 3). We assume that the lower-intensity population is due to the RNA strands and the higher-intensity population is due to the MS2 viruses. To determine the median and width of each intensity population, we separate the two using an intensity threshold (0.003) that lies between them.

Assembly experiments. For assembly experiments, we fill a flow cell with hybridization buffer containing 0.2% Tween-20 (Sigma-Aldrich) and let it sit for 10 min. We find that this 10-min incubation with Tween-20 prevents the MS2 coat protein from adsorbing to the coverslip through defects in the PEG layer. Next, we flush out the Tween-20 with fresh hybridization buffer, find the center of the imaging chamber, focus the microscope onto the coverslip, and begin the out-of-plane active stabilization control loop. Then we locate a 30-nm gold particle within 50 μ m of the center of the imaging chamber and start the in-plane active stabilization control loop. With the setup actively stabilized in all three dimensions, we inject 1 nM RNA-DNA complexes in hybridization buffer and record a short movie of them adsorbing to the coverslip. After 10–100 complexes bind, we flush the imaging chamber by

pumping 120 μL of assembly buffer through the chamber over the course of 12 min. Then we start recording a movie and inject the coat-protein dimers in assembly buffer. The injection starts 4 s into the movie.

Image processing. We process the images to normalize them and to reduce fluctuations in the background intensity. We apply an approach similar to the ‘pseudo-flat-fielding’ method described by Ortega-Arroyo and coworkers³⁵. The images in Fig. 1, and Extended Data Fig. 3, are processed in this way, as are all the movies included in the Supplementary Information.

Each raw image, denoted I_{raw} , is processed according to the following steps: First, a dark image, I_{dark} , is acquired by taking the time-median of many frames (200 frames for 100 Hz data and 2,000 for 1,000 Hz data) when the illumination beam is blocked. This image is subtracted from each raw image, yielding $I_{\text{bkgd}} = I_{\text{raw}} - I_{\text{dark}}$. Second, features bigger than $\sigma_1 = 1.5$ pixels are removed by subtracting a Gaussian blur, yielding $I_{\text{smooth}} = I_{\text{bkgd}} - \text{blur}(I_{\text{bkgd}}, \sigma_1)$, where $\text{blur}(I, \sigma)$ is 2D Gaussian blur of the image, I , using a standard deviation σ . We choose $\sigma_1 = 1.5$ to minimize intensity changes that arise from time-varying background fringes, even though this choice slightly decreases the normalized intensities of the particles on the coverslip. Third, the image is normalized to the background that has been blurred with $\sigma_2 = 20$ pixels, so that particles on the coverslip and stray fringes smaller than σ_2 do not affect the normalization. This process yields $I_{\text{norm}} = (I_{\text{smooth}})/\text{blur}(I_{\text{bkgd}}, \sigma_2)$. Because each image is normalized independently of other images in the time-series, fluctuations in the illumination intensity in time do not affect I_{norm} . Finally, all remaining static features in the background are removed by subtracting the time-median of many frames (300 frames for 100 Hz data and 3,000 for 1,000 Hz data) of the movie, yielding the final processed image $I_{\text{final}} = I_{\text{norm}} - I_{\text{norm,med}}$. The noise in I_{final} is set by shot noise for the first few seconds after the background subtraction, but after this time, fluctuations in the background intensity due to uncorrected mechanical drift are the main source of measurement noise.

Identifying and measuring assembling particles. To identify assembling particles, we manually locate the centers of all dark spots that appear and are between 1 and 4 pixels across in each processed interferometric scattering movie. We repeat this procedure multiple times using different frames for the background subtraction to ensure that no dark spots are missed. For each of these spots, we measure the mean intensity in a circle of radius 1 pixel that is centered on the particle as a function of time.

We reject any spot that: (1) instantaneously appears in the movie, indicating that it is from a particle that has adsorbed to the coverslip; (2) is near the gold particle used for active stabilization or near a defect on the coverslip that has comparable intensity (greater than 0.1); (3) is near a particle that adsorbs to or desorbs from the coverslip, such that its intensity is altered by the particle; (4) is so close to another spot that the interference fringes of the two spots overlap; (5) is near the edge of the field of view; or (6) grows

at a slow and consistent rate over the course of the measurement, consistent with protein assembly in the absence of RNA. We describe how each of these criteria are applied in the Supplementary Information.

Determining start and growth times. The cumulative distribution functions of the start times before assembly (Figs. 2 and Extended Data Figs. 5) are measured as follows. Each start time is defined as the time at which a kinetic trace reaches an intensity of 0.001. To measure this time, we smooth each trace using a 1,000-frame moving average. The first time that the smoothed trace reaches an intensity greater than 0.001 is called t_1 , and the last time that the smoothed trace has an intensity less than 0.001 is called t_2 (ignoring any late detachment events or drifts in intensity). The start time is then determined as $t_{\text{start}} = (t_1 + t_2)/2$. To estimate the uncertainty in each start time, we calculate the half-width of the moving-average window and $(t_2 - t_1)/2$, and we take the greater of the two. The cumulative distribution function of start times is obtained by sorting the measured values of t_{start} .

We then fit the cumulative distribution to the exponential function $N(t) = A(1 - \exp[-(t - t_0)/\tau])$ using a Bayesian parameter-estimation framework. A uniform, unbounded prior is used for all parameters. The exponential function is first inverted, yielding

$$(1) \quad t(N) = t_0 - \tau \ln(1 - N/A),$$

where the fit parameters are t_0 , A , and τ . The posterior probability distribution $p(t_0, A, \tau \mid D_{\text{CDF}}, M)$, where D_{CDF} is the observed cumulative distribution function and M is the model (Equation (1)), is then sampled using an affine-invariant ensemble Markov-chain Monte Carlo sampler⁴² with 50 walkers that take 500 steps each. The walkers are initially distributed in a narrow Gaussian around the peak of the posterior probability density function. The position of the peak is calculated from a least-squares fit to $t(N)$. The walkers reach an equilibrium distribution after approximately 200 steps. Pair plots of the positions of the walkers on every step after the burn-in are shown in Extended Data Fig. 5, along with the marginal distributions for each fit parameter. The best-fit parameters reported in the text are taken as the 50th percentile of the marginal distributions, and the reported uncertainties represent a credibility interval from the 16th to the 84th percentile.

To determine the growth time we first take the portion of each kinetic trace that lies between the start time and the time at which the intensity first reaches the 10th percentile of the capsid intensity distribution (Extended Data Fig. 3), and fit this portion of the trace to a line, using a least-squares method. We then estimate the time required to grow a full capsid (bind 90 dimers) by approximating the growth rate as the slope of the linear fit.

Control assembly experiment with lower illumination intensity. To test whether the intensity of the incident beam affects the assembly process, we perform a set of duplicate control experiments with 2 μM coat-protein dimers and a light intensity that is 10-fold smaller (approximately

0.3 kW/cm²). The results, shown in the Supplementary Information, indicate that the incident light does not qualitatively affect the assembly process.

TEM of assembled particles. We use negative staining and TEM to im- 450
age the protein structures that form on MS2 RNA. First, we describe assembly experiments with MS2 RNA that is tethered to the surface of 30-nm gold particles (Fig. 2e, Extended Data Fig. 4). The surfaces of the gold particles are functionalized in a way that is similar to that used for the coverslips. The protocol is identical to that used to prepare the tracer particles for active 455
stabilization (Supplementary Information), except that we use NHS-PEG-N₃ instead of NHS-PEG. To conjugate DNA oligonucleotides to the PEG-coated gold particles, we add 5 μ M DBCO-DNA to 10 nM gold particles in PBS without Ca or Mg. The mixture is left at room temperature overnight in a tube rotator and then washed 5 times by centrifuging the mixture at 8,000 460
g for 5 min and resuspending in TE buffer.

To perform the assembly reaction, we add a 100-fold molar excess of RNA-DNA complexes (20 nM) to the gold particles (0.2 nM) and equilibrate the mixture in TNE buffer for 1 hr on ice. We then take 6 μ L of this mixture, 465
add 0.42 μ L of 30 μ M coat-protein dimers suspended in 20 mM acetic acid, and let the mixture sit for 10 min at room temperature. The mixture is then added to a plasma-etched carbon-coated TEM grid (Ted Pella), left to sit for 1 min, and then removed by blotting with filter paper. Then 6 μ L of methylamine tungstate stain solution (Nanoprobes) is added and left to sit for 1 min before removal by blotting with filter paper. We visualize the 470
samples on a Tecnai F20 (FEI) transmission electron microscope operated at 120 kV. Images are captured on a 4,096 \times 4,096-pixel CCD camera (Gatan). Representative images are shown in Extended Data Fig. 4 along with images of control reactions involving bare RNA without the DNA linkage.

We also perform assembly reactions with RNA that is free in solution. 475
This is done by mixing varying concentrations of coat protein with 10 nM of RNA in assembly buffer. After allowing the assembly reaction to proceed for a fixed amount of time, the mixture is imaged by TEM, as described above. Representative electron micrographs of particles assembled with 1.5, 2, and 4 μ M coat-protein dimers are shown in Extended Data Fig. 9. 480

Buffer recipes.

Assembly buffer: 42 mM Tris-HCl, pH 7.5; 84 mM NaCl; 3 mM acetic acid; 1 mM EDTA

Hybridization buffer: 50 mM Tris-HCl, pH 7.0; 200 mM NaCl; 1 mM EDTA 485

TAE buffer: 40 mM Tris-acetic acid, pH 8.3; 1 mM EDTA

TNE buffer: 50 mM Tris-HCl, pH 7.5; 100 mM NaCl; 1 mM EDTA

TE buffer: 10 mM Tris-HCl, pH 7.5; 1 mM EDTA

Code availability. The code used to analyze the data is available from the corresponding author on reasonable request. 490

Data availability. The datasets generated and analyzed during the current study are available from the corresponding author on reasonable request.

ACKNOWLEDGEMENTS

We thank Peter Stockley and Amy Barker at the University of Leeds for sending us initial stocks of MS2 virus and C3000 cells and their growth protocols. We thank Philip Kukura, Marek Piliarik, Vahid Sandoghdar, and Michael Brenner for helpful discussions. This work is supported by the Harvard MRSEC under National Science Foundation grant no. DMR-1420570. Additionally, this material is based upon work supported in part by the National Science Foundation Graduate Research Fellowship under grant no. DGE-1144152. It was performed in part at the Center for Nanoscale Systems (CNS), a member of the National Nanotechnology Coordinated Infrastructure Network (NNCI), which is supported by the National Science Foundation under NSF award no. 1541959. CNS is part of Harvard University.

AUTHOR CONTRIBUTIONS

VNM came up with the idea of studying virus self-assembly using interferometric scattering microscopy and developed this idea with RFG and AMG. AMG and RFG designed the experimental setup, performed the experiments, and analyzed the data. VNM supervised the project. AMG, RFG, and VNM wrote the manuscript.

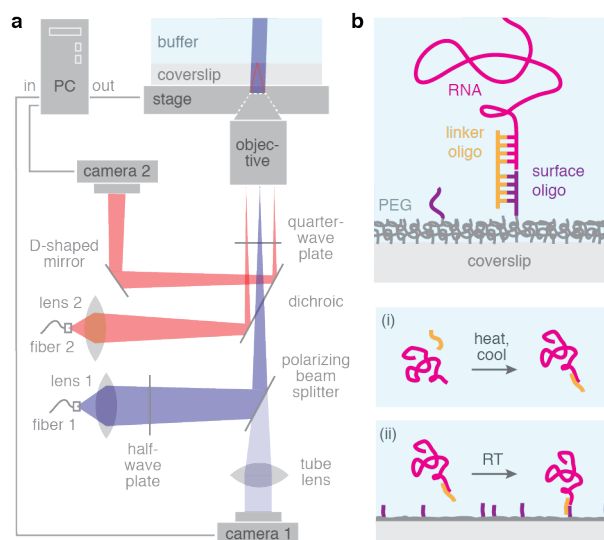
REFERENCES

- [1] Caspar, D. L. D.; Klug, A. *Cold Spring Harbor Symposia on Quantitative Biology* **1962**, *27*, 1–24.
- [2] Bancroft, J. B.; Hiebert, E. *Virology* **1967**, *32*, 354–356.
- [3] Harrison, S. C.; Olson, A. J.; Schutt, C. E.; Winkler, F. K.; Bricogne, G. *Nature* **1978**, *276*, 368.
- [4] Fisher, A. J.; Johnson, J. E. *Nature* **1993**, *361*, 176.
- [5] Dai, X.; Li, Z.; Lai, M.; Shu, S.; Du, Y.; Zhou, Z. H.; Sun, R. *Nature* **2017**, *541*, 112–116.
- [6] Berger, B.; Shor, P. W.; Tucker-Kellogg, L.; King, J. *Proceedings of the National Academy of Sciences* **1994**, *91*, 7732–7736.
- [7] Schwartz, R.; Shor, P. W.; Prevelige Jr, P. E.; Berger, B. *Biophysical Journal* **1998**, *75*, 2626–2636.
- [8] Elrad, O. M.; Hagan, M. F. *Physical Biology* **2010**, *7*, 045003.
- [9] Perlmutter, J. D.; Perkett, M. R.; Hagan, M. F. *Journal of Molecular Biology* **2014**, *426*, 3148–3165.
- [10] Dykeman, E. C.; Stockley, P. G.; Twarock, R. *Proceedings of the National Academy of Sciences* **2014**, *111*, 5361–5366.
- [11] Jacobsen, V.; Stoller, P.; Brunner, C.; Vogel, V.; Sandoghdar, V. *Optics Express* **2006**, *14*, 405–414.
- [12] Young, G. et al. *Science* **2018**, *360*, 423–427.

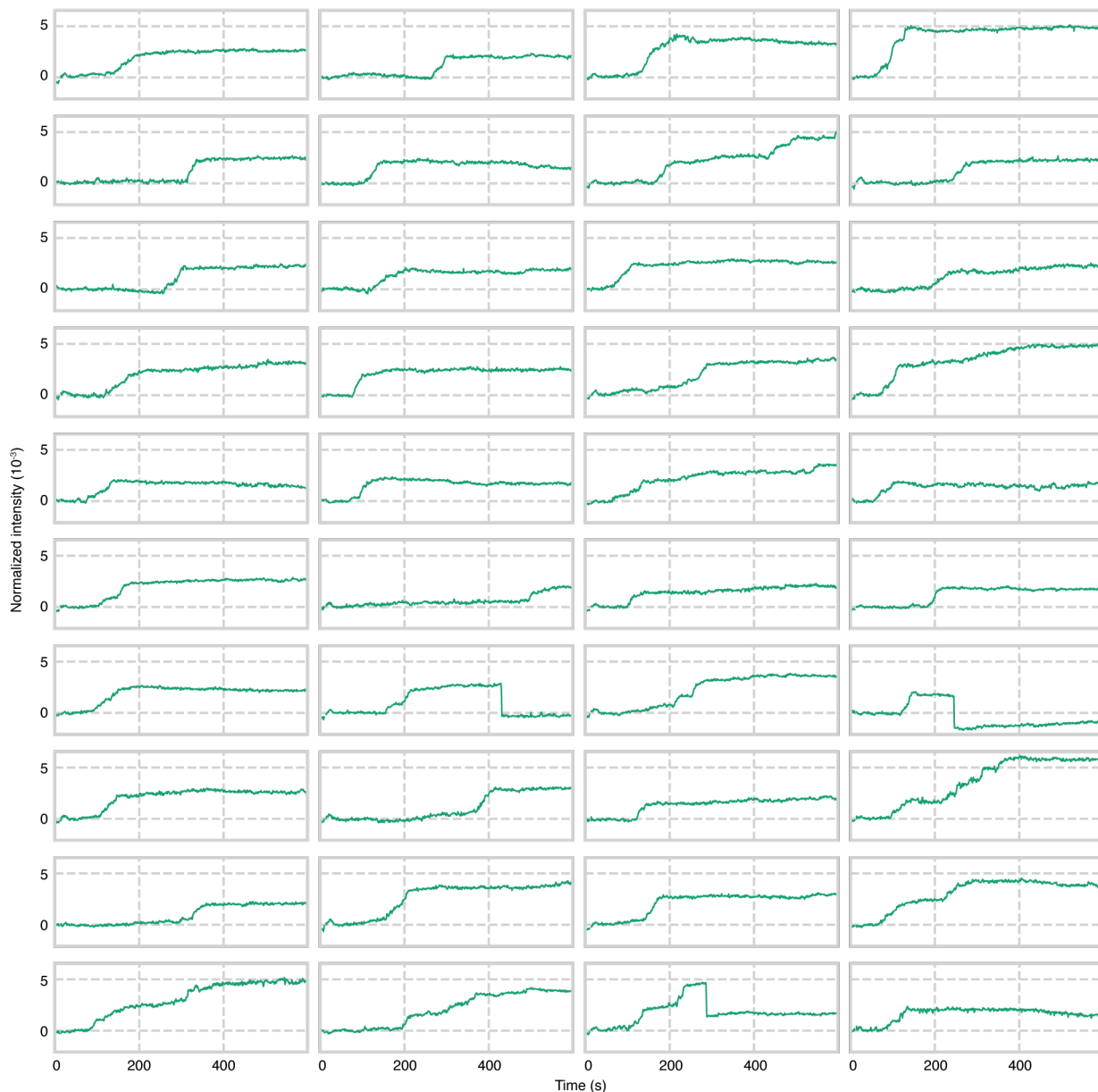
- [13] Butterfield, G. L.; Lajoie, M. J.; Gustafson, H. H.; Sellers, D. L.; Nattermann, U.; Ellis, D.; Bale, J. B.; Ke, S.; Lenz, G. H.; Yehdego, A.; Ravichandran, R.; Pun, S. H.; King, N. P.; Baker, D. *Nature* **2017**, *552*, 415. 535
- [14] Deres, K. et al. *Science* **2003**, *299*, 893–896.
- [15] Garmann, R. F.; Sportsman, R.; Beren, C.; Manoharan, V. N.; Knobler, C. M.; Gelbart, W. M. *Journal of the American Chemical Society* **2015**, *137*, 7584–7587.
- [16] Sugiyama, T.; Hebert, R. R.; Hartman, K. A. *Journal of Molecular Biology* **1967**, *25*, 455–463. 540
- [17] Toropova, K.; Basnak, G.; Twarock, R.; Stockley, P. G.; Ranson, N. A. *Journal of Molecular Biology* **2008**, *375*, 824–836.
- [18] Hohn, T. *Journal of Molecular Biology* **1969**, *43*, 191–200.
- [19] Romaniuk, P. J.; Lowary, P.; Wu, H. N.; Stormo, G.; Uhlenbeck, O. C. *Biochemistry* **1987**, *26*, 1563–1568. 545
- [20] Beckett, D.; Wu, H.-N.; Uhlenbeck, O. C. *Journal of Molecular Biology* **1988**, *204*, 939 – 947.
- [21] Stockley, P. G.; Rolfsson, O.; Thompson, G. S.; Basnak, G.; Francese, S.; Stonehouse, N. J.; Homans, S. W.; Ashcroft, A. E. *Journal of Molecular Biology* **2007**, *369*, 541–552. 550
- [22] Borodavka, A.; Tuma, R.; Stockley, P. G. *Proceedings of the National Academy of Sciences* **2012**, *109*, 15769–15774.
- [23] Sorger, P. K.; Stockley, P. G.; Harrison, S. C. *Journal of Molecular Biology* **1986**, *191*, 639–658. 555
- [24] Kler, S.; Wang, J. C.-Y.; Dhason, M.; Oppenheim, A.; Zlotnick, A. *ACS Chemical Biology* **2013**, *8*, 2753–2761.
- [25] Garmann, R. F.; Comas-Garcia, M.; Gopal, A.; Knobler, C. M.; Gelbart, W. M. *Journal of Molecular Biology* **2014**, *426*, 1050–1060.
- [26] Zandi, R.; van der Schoot, P.; Reguera, D.; Kegel, W.; Reiss, H. *Biophysical Journal* **2006**, *90*, 1939–1948. 560
- [27] Prevelige Jr, P. E.; Thomas, D.; King, J. *Biophysical Journal* **1993**, *64*, 824.
- [28] Zlotnick, A.; Johnson, J. M.; Wingfield, P. W.; Stahl, S. J.; Endres, D. *Biochemistry* **1999**, *38*, 14644–14652. 565
- [29] Medrano, M.; Fuertes, M. Á.; Valbuena, A.; Carrillo, P. J. P.; Rodríguez-Huete, A.; Mateu, M. G. *Journal of the American Chemical Society* **2016**, *138*, 15385–15396.
- [30] Lavelle, L.; Gingery, M.; Phillips, M.; Gelbart, W. M.; Knobler, C. M.; Cadena-Nava, R. D.; Vega-Acosta, J. R.; Pinedo-Torres, L. A.; Ruiz-Garcia, J. *The Journal of Physical Chemistry B* **2009**, *113*, 3813–3819. 570
- [31] Pierson, E. E.; Keifer, D. Z.; Kukreja, A. A.; Wang, J. C.-Y.; Zlotnick, A.; Jarrold, M. F. *Journal of Molecular Biology* **2016**, *428*, 292–300.
- [32] De Yoreo, J. *Nature Materials* **2013**, *12*, 284. 575
- [33] Prevelige, P. E. *Journal of Molecular Biology* **2016**, *2*, 416–418.

- [34] Song, Y.; Gorbatshevych, O.; Liu, Y.; Mugavero, J.; Shen, S. H.; Ward, C. B.; Asare, E.; Jiang, P.; Paul, A. V.; Mueller, S.; Wimmer, E. *Proceedings of the National Academy of Sciences* **2017**, *114*, E8731–E8740. 580
- [35] Ortega-Arroyo, J.; Cole, D.; Kukura, P. *Nature Protocols* **2016**, *11*, 617–633.
- [36] Dulin, D.; Barland, S.; Hachair, X.; Pedaci, F. *PLOS ONE* **2014**, *9*, 1–9.
- [37] Moerner, W.; Fromm, D. P. *Review of Scientific Instruments* **2003**, *74*, 3597–3619. 585
- [38] Allan, D.; Caswell, T.; Keim, N.; van der Wel, C. Trackpy v0.3.2. 2016; <https://doi.org/10.5281/zenodo.60550>.
- [39] Joo, C.; Ha, T. *Cold Spring Harbor Protocols* **2012**, 1223–1237.
- [40] Strauss, J. H.; Sinsheimer, R. L. *Journal of Molecular Biology* **1963**, *7*, 43 – 54. 590
- [41] Goldfain, A. M.; Garmann, R. F.; Jin, Y.; Lahini, Y.; Manoharan, V. N. *The Journal of Physical Chemistry B* **2016**, *120*, 6130–6138.
- [42] Foreman-Mackey, D.; Hogg, D. W.; Lang, D.; Goodman, J. *Publications of the Astronomical Society of the Pacific* **2013**, *125*, 306. 595

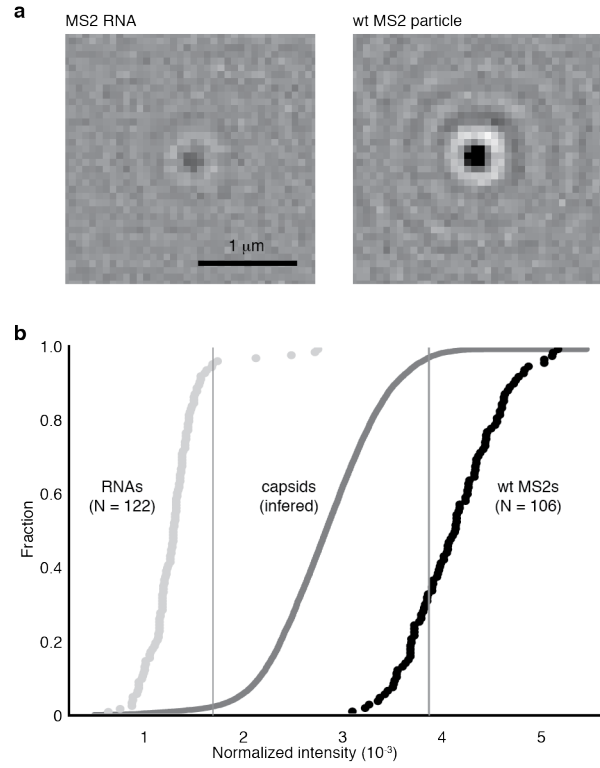
EXTENDED DATA



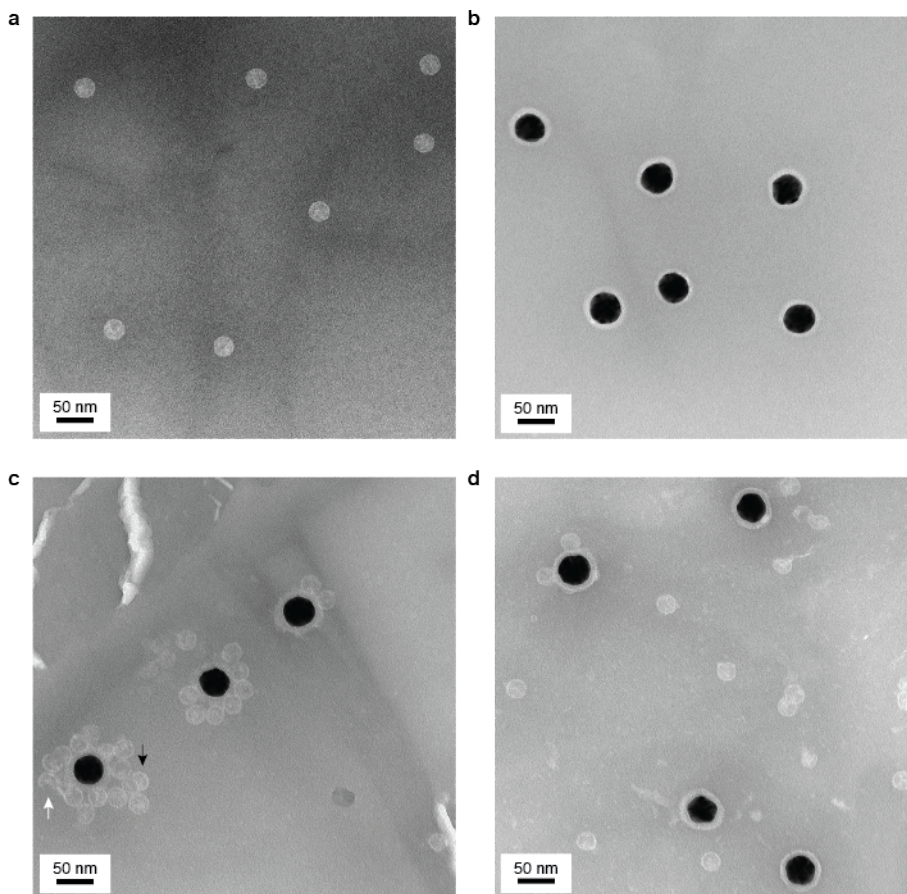
EXTENDED DATA FIGURE 1. Diagram of the interferometric scattering microscope and DNA linkages. (a) Our microscope is similar to the setup described by Ortega-Arroyo and coworkers³⁵. 450-nm light (blue) is used for illumination. 785-nm light (red) is used for active stabilization in the dimension perpendicular to the coverslip surface. Details of the instrument are described in Methods. (b) We use DNA linkages¹⁵ to bind MS2 RNA to the surface of a microscope coverslip. Top: diagram of the basepairing between the 5'-end of the RNA, a linker oligo, and a surface oligo that is covalently bound to the PEG-functionalized coverslip. Bottom: to construct the linkages we (i) bind the RNA to the linker oligo in solution by thermal annealing, and then (ii) add the RNA-DNA complexes to the functionalized coverslips at room temperature. Details of the process are described in Methods.



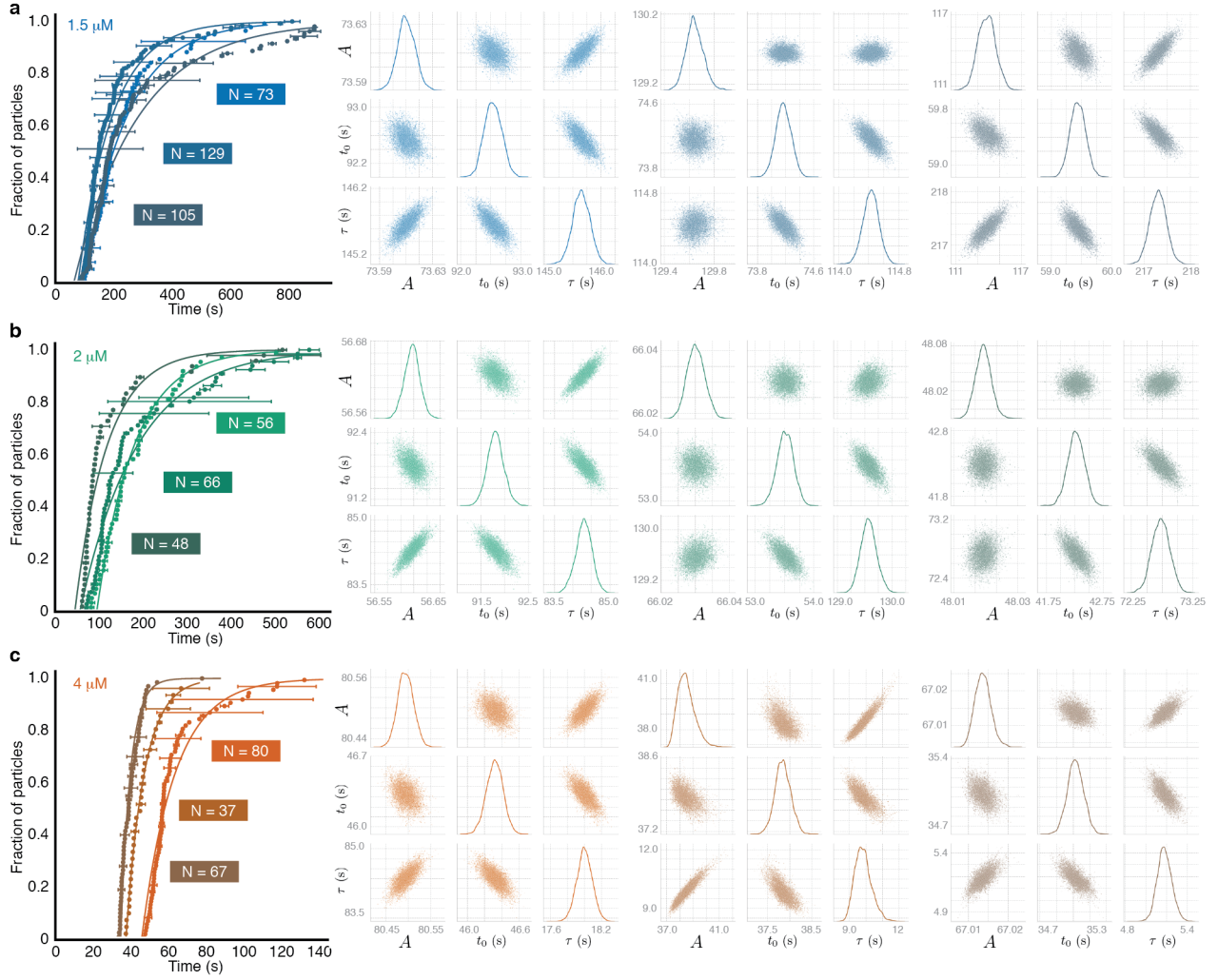
EXTENDED DATA FIGURE 2. Assembly of 2 μM coat-protein dimers. Kinetic traces for 40 of the 56 observed assembling particles in one experiment are shown. Some traces show abrupt drops in intensity, which we interpret as detachment events. One of the above traces drops to an intensity of between -0.001 and -0.002, which is approximately the negative intensity of the RNA in the background image. We therefore interpret this event as the detachment of the RNA and assembled proteins from the surface. One trace drops to an intensity near 0, suggesting that the assembled protein has detached from the RNA, while the RNA remains on the surface. One of the traces drops from an intensity near 0.005 by an amount (0.0032) that corresponds to a full capsid, suggesting that overgrown particles can contain capsids. A portion of the traces from the same experiment appear in Fig. 2, and one trace from the experiment appears in Fig. 1d. The final intensities of the particles in this experiment are used for Fig. 3c. The traces are measured from the data shown in Supplementary Movie 1. The data are recorded at 1,000 Hz and are plotted with a 1,000-frame average.



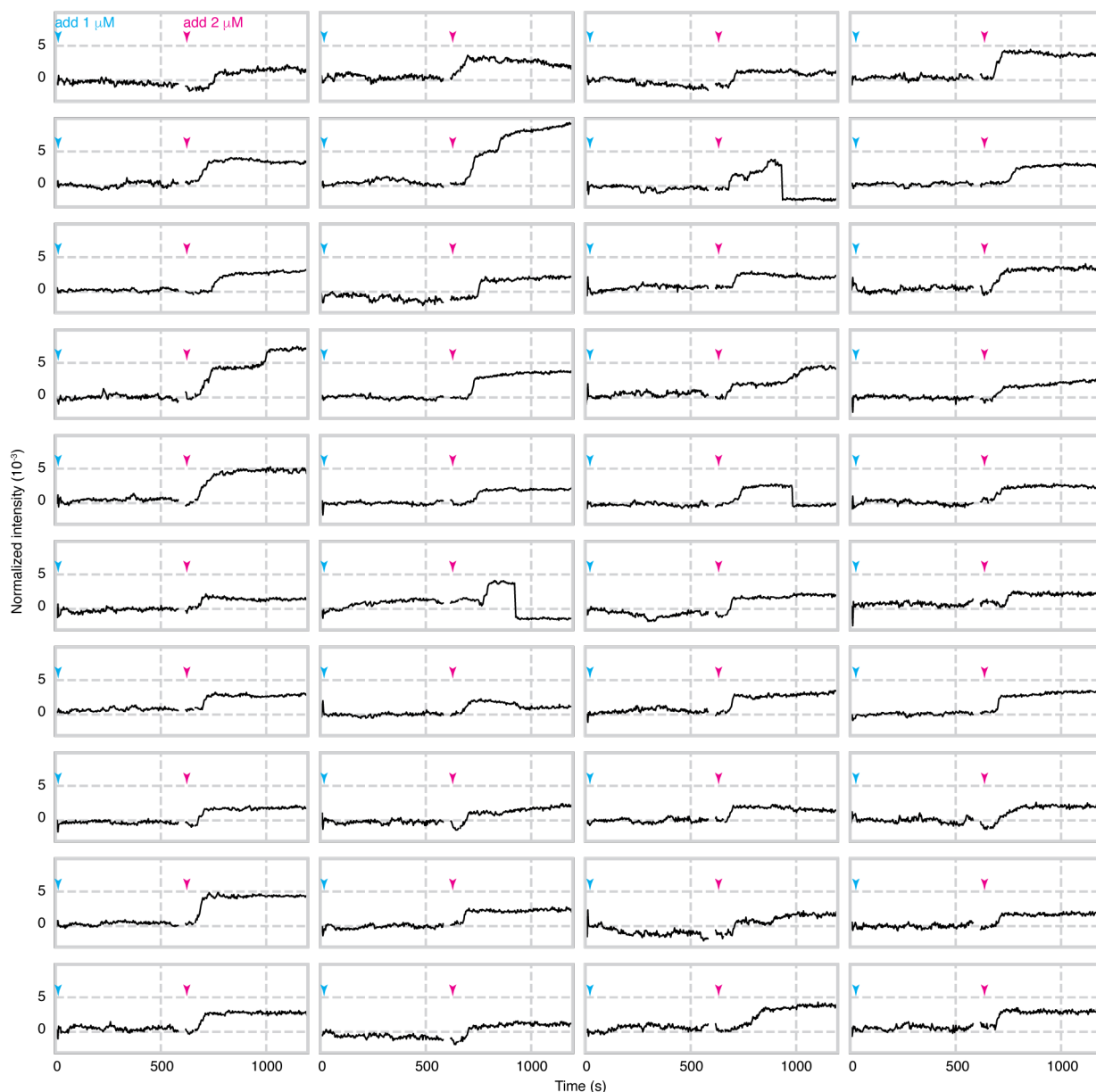
EXTENDED DATA FIGURE 3. Cumulative distribution of the normalized intensities of MS2 RNA strands and wild-type MS2 virus particles measured in the interferometric scattering microscope. See Methods for details of the measurement. (a) Images of a single MS2 RNA strand (left) and a single wild-type MS2 virus particle (right). Both images are recorded at 100 Hz and shown with a 300-frame average. (b) We infer the cumulative distribution of intensities for MS2 capsids that fully assemble on surface-tethered RNA by convolving the intensity distribution of the wild-type MS2 particles with the negative of the intensity distribution of the MS2 RNA strands. The gray lines, which mark where the capsid distribution reaches 2.3% and 97.7%, denote the interval we use for identifying full capsids in the kinetic traces.



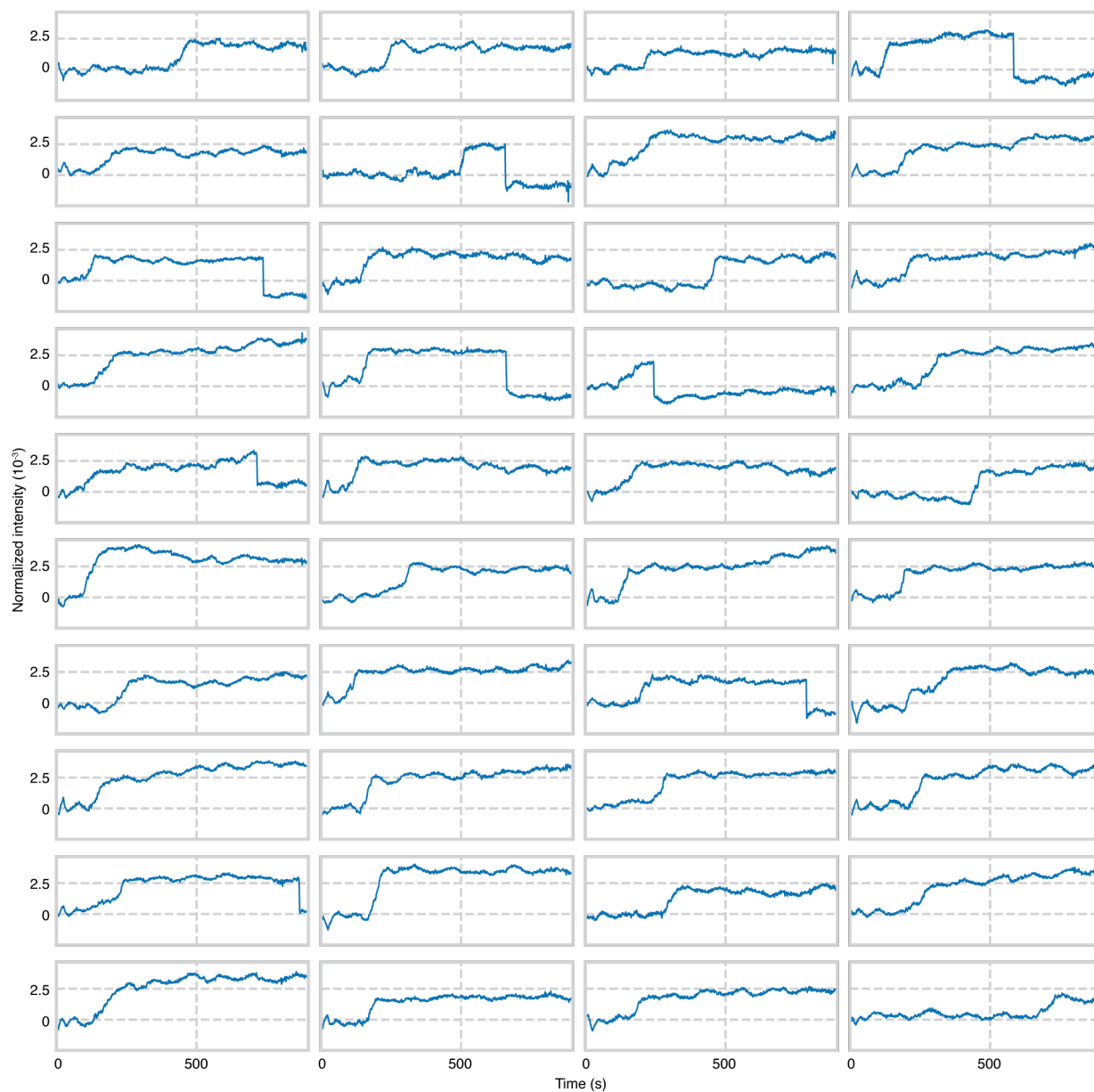
EXTENDED DATA FIGURE 4. Negatively stained transmission electron micrographs of virus particles, functionalized gold nanoparticles, capsids assembled around RNA strands that are bound to the surface of the gold particles, and capsids assembled around untethered RNA. Each sample is stained with methylamine tungstate stain solution (Nanoprobes) before imaging. (a) Wild-type MS2 particles. (b) Amine-functionalized 30-nm gold nanoparticles (Nanopartz) that are coated with PEG and decorated with surface oligos. The dark spots are the gold particles, and the surrounding lighter halos are the negatively stained coatings on the particle surfaces. These coatings consist of a proprietary polymer base layer, which is applied by the manufacturer to the gold nanoparticles, and the PEG-DNA molecules that we conjugate to the particles. (c) An assembly reaction in which 2 μ M coat-protein dimers in assembly buffer is added to RNA-DNA complexes that have been incubated for 1 h with the functionalized gold particles. White arrow points to a partial capsid. Black arrow points to a particle that is larger than a capsid. (d) A control reaction in which 2 μ M coat-protein dimers in assembly buffer is added to bare RNA that has been incubated for 1 h with the functionalized gold particles. The higher number of capsids near the surface of the gold particles for the experiments using RNA-DNA complexes suggests that these capsids assembled around RNA-DNA complexes that were tethered to the particle surface.



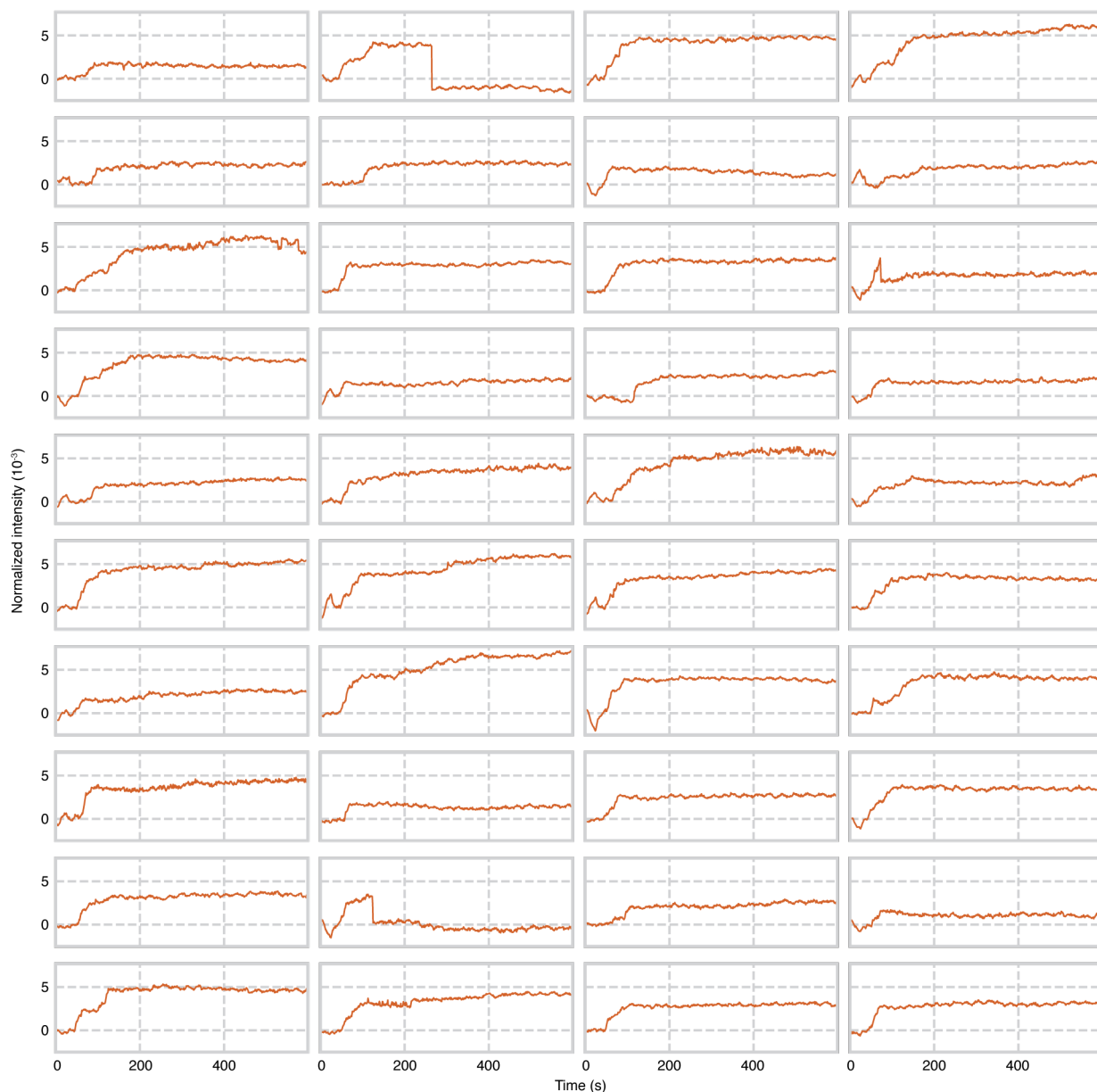
EXTENDED DATA FIGURE 5. Cumulative distributions of start times and posterior probability distributions of parameter values obtained by fitting the distributions. The results from triplicate assembly experiments with (a) 1.5, (b) 2, and (c) 4 μM dimers are shown. Each cumulative distribution of start times (left) is measured from a separate assembly experiment. Uncertainties in the time measurements are represented by horizontal bars. Fits are shown as solid curves. Number of particles (N) are shown on the plot. Posterior probability distributions of parameter values (right) are sampled using a Markov-chain Monte Carlo technique. The plots along the diagonal show kernel density estimates of the fully marginalized posterior distributions of each parameter, while the off-diagonal plots show the joint distributions. The data and fit shown in the lightest color of each panel are from the experiments shown in Figs. 2, 3a, 3c, and Extended Data Figs. 7 and 8. Data from all 9 of the experiments in this figure were used to obtain the nucleation times shown in Fig. 3b.



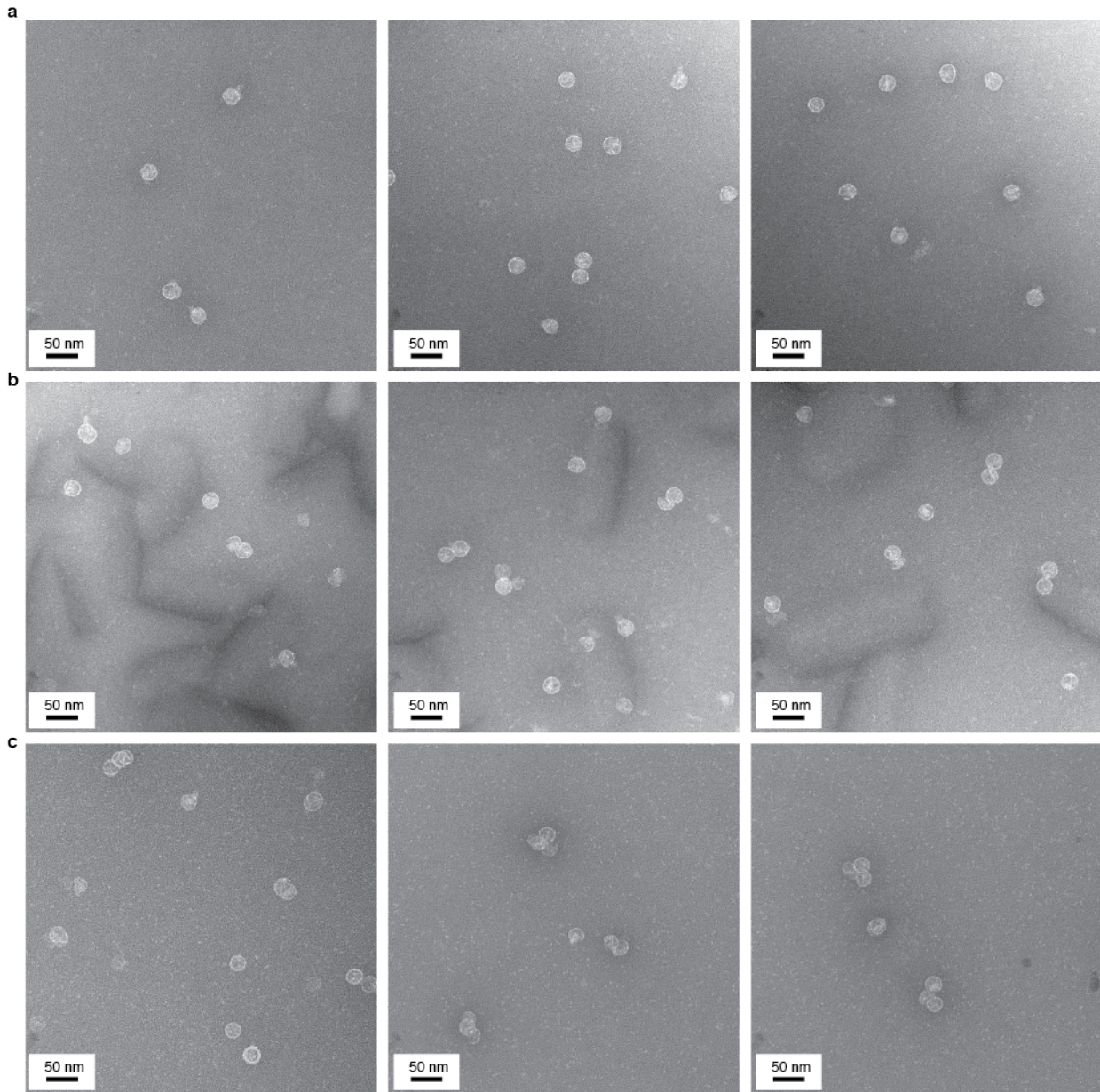
EXTENDED DATA FIGURE 6. Assembly of 1 μM coat-protein dimers. When 1 μM coat-protein dimers is added (cyan arrowheads) to the surface-bound RNA, no assembling particles appear over the course of 600 s. At this point, 2 μM coat-protein dimers is added (pink arrowheads), after which we observe particles assembling at 75 locations within the field of view. Intensity traces for 40 of these particles are shown above. We also show traces for the first 600 s at the same locations. There is no data between 586 and 615 s, during which time we block the illumination beam and inject the 2 μM protein. As in Extended Data Fig. 2, we interpret abrupt drops in intensity after assembly as detachment events. The traces are measured from the data shown in Supplementary Movie 2. The data are recorded at 100 Hz and are plotted with a 300-frame average.



EXTENDED DATA FIGURE 7. Assembly of 1.5 μ M coat-protein dimers. Kinetic traces for 40 of the 73 observed assembling particles in one experiment are shown. As in Extended Data Fig. 2, we interpret abrupt drops in intensity after assembly as detachment events. A portion of the traces from the same experiment appear in Fig. 3. The final intensities of the particles in this experiment are used for Fig. 3c. The traces are measured from the data shown in Supplementary Movie 3. The data are recorded at 1,000 Hz and are plotted with a 1,000-frame average.



EXTENDED DATA FIGURE 8. Assembly with 4 μ M coat-protein dimers. Kinetic traces for 40 of the 80 observed assembling particles in one experiment are shown. As in Extended Data Fig. 2, we interpret abrupt drops in intensity after assembly as detachment events. A portion of the traces from the same experiment appear in Fig. 3. The final intensities of the particles in this experiment are used for Fig. 3c. The traces are measured from the data shown in Supplementary Movie 4. The data are recorded at 1,000 Hz and are plotted with a 1,000-frame average.



EXTENDED DATA FIGURE 9. Negatively stained transmission electron micrographs of assembled particles from control experiments performed with varying concentrations of protein and untethered RNA. Each sample is stained with methylamine tungstate stain solution (Nanoprobes) before imaging. (a) Three micrographs of particles taken 20 min after mixing 1.5 μM coat-protein dimers and 10 nM RNA in assembly buffer. (b) Three micrographs of particles taken 10 min after mixing 2 μM coat-protein dimers and 10 nM RNA in assembly buffer. (c) Three micrographs of particles taken 10 min after mixing 4 μM coat-protein dimers and 10 nM RNA in assembly buffer.

SUPPLEMENTARY INFORMATION FOR MEASUREMENTS OF THE SELF-ASSEMBLY KINETICS OF INDIVIDUAL VIRAL CAPSIDS AROUND THEIR RNA GENOME

REES F. GARMANN^{1,†}, AARON M. GOLDFAIN^{1,†}, AND VINOTHAN N.
MANOHARAN^{1,2}

TIME FOR PROTEIN TO REACH THE SURFACE-BOUND RNA

Here we estimate how long it takes MS2 coat-protein dimers to reach the surface-bound RNA molecules after the protein is pumped into the imaging chamber. This time scale is set by the rate of diffusion and the distance between the protein and coverglass when it is first introduced.

We first model how fluid is introduced into the imaging chamber. Downstream of the inlet cup, the flow cell contains a cylindrical inlet chamber (1 mm diameter, 3 mm long), which is followed by the imaging chamber (0.75 mm tall, 1.0 mm wide, and 4.6 mm long) that contains our field of view. The field of view is in the center of the bottom surface of the imaging chamber. To simplify our calculations, we assume that the flow cell consists of a single cylindrical chamber with a radius $R = 0.375$ mm and that our field of view is $L = 9.3$ mm from the entrance to the cylinder. The diameter of the cylinder is chosen to match the height of the imaging chamber, and the length L is chosen so that the volume πLR^2 is the same as the total volume in the actual inlet and imaging chambers upstream of the field of view.

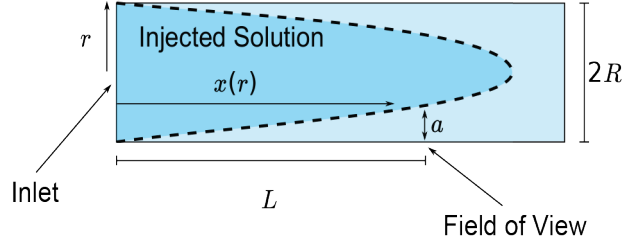
We assume a no-slip boundary condition, such that the flow profile in the model cylindrical chamber is laminar and parabolic¹. In our experiments, we inject $V = 10$ μL of fluid over 20 s, so that the average flow velocity is approximately 0.5 mm/s, yielding a Reynolds number of 0.5, which justifies the laminar assumption. We further assume that the diffusion of protein across the chamber is negligible over the duration of the pumping, so that the parabolic front that separates the new protein solution from the old buffer solution is sharply defined. Indeed, the time for an MS2 coat-protein dimer (hydrodynamic radius 2.5 nm (Ref. 2) with diffusion coefficient, $D = 90$ $\mu\text{m}^2/\text{s}$) to diffuse across the cylinder radius is approximately 1,600 s, much

¹HARVARD JOHN A. PAULSON SCHOOL OF ENGINEERING AND APPLIED SCIENCES, CAMBRIDGE, MA 02138 USA

²DEPARTMENT OF PHYSICS, HARVARD UNIVERSITY, CAMBRIDGE, MA 02138 USA

[†]EQUAL CONTRIBUTION

E-mail address: vnm@seas.harvard.edu.



SUPPLEMENTARY FIGURE 1. Model of the flow profile for the injected protein. We model the flow chamber as a cylinder, as discussed in Methods. The dashed line represents the parabolic boundary between the injected protein solution and the solution that is already in the chamber.

longer than the pumping duration. The shape of the parabolic boundary is described by $x(r) = (2V/\pi R^2) (1 - (r/R)^2)$, where r is the radial coordinate of the cylinder, and $x(r)$ is the distance down the cylinder from the end where the protein is injected (Supplementary Figure 1). Note that in the center of the cylinder, $x(r = 0) \approx 45$ mm. Thus, the tip of the parabola following a pump of $V = 10$ μL extends well beyond the field of view. Above the field of view, the distance from the parabolic boundary to the surface is $a = R(1 - \sqrt{1 - \pi R^2 L / 2V}) \approx 40$ μm . This is the distance that the protein must diffuse to reach the surface-bound RNA.

To experimentally determine the distance from the parabolic boundary to the surface just after the pump, we use a bright-field microscope (Eclipse Ti, Nikon) and tracer particles (1 μm sulfate-latex, Invitrogen). For this experiment we fill the flow cell with water, position our field of view in the center of the imaging chamber, inject a solution of tracer particles (0.08% w/v in water), and measure the distance of the tracer particles from the coverslip immediately after the injection. We find that there is a well-defined boundary between the solutions with and without particles, and that this boundary is $a = 20$ – 50 μm above the coverslip, depending on the pump and flow cell used. This distance agrees well with the distance calculated above (40 μm).

With this length scale and the diffusion coefficient, we can calculate the time it takes proteins to diffuse to the surface, $t_D = a^2/D$. More specifically, at a distance a from the protein solution, t_D is the time it takes for the concentration of proteins to reach approximately half the injected concentration. We find that, for a 20–50 μm distance, $t_D = 5$ – 30 s.

This timescale agrees with the measured delay time that precedes assembly in our experiments. For our assembly experiments, we stop pumping 24 s after the time-series begins, so the concentration of protein at the surface should reach half of the injected concentration about 30–55 s after the

beginning of the time-series. Since we do not observe assembly on our experimental time scales when introducing 1 μM protein dimers (Extended Data Figure 6), we do not expect to detect assembling particles until after the concentration of dimers at the surface exceeds 1 μM . Thus, when introducing 1.5 μM dimers, we do not expect to detect assembling particles until after this 30–55 s delay, which is indeed the case (Extended Data Figure 5). Also, when introducing 2 μM and 4 μM protein dimers, we expect to detect assembling particles a bit sooner but not before this 30–55 s delay, which is again what we observe (Extended Data Figure 5).

CONFIGURATION OF THE INTERFEROMETRIC MICROSCOPE

In our microscope, the imaging beam is slightly misaligned to reduce back-reflections from the objective and the roof of the imaging chamber. To keep the point-spread function of the microscope symmetric, we set the misalignment as small as possible such that back-reflections from the objective do not overlap with the reference beam on the camera. To accomplish this, we first align the imaging beam with the microscope axis, and then we offset fiber 1 laterally using a two-axis linear translation stage (Thorlabs) and tilt the imaging beam using a mirror mounted in a two-axis kinematic mount (Thorlabs) located between lens 1 and the half-wave plate.

To minimize vibrations and long-term mechanical drift, we make the imaging beam path as short as possible, we mount the apparatus on an isolated optical table (RS4000, Newport), and we secure all cables going to non-isolated equipment using clamps that we line with semi-rigid foam (0.75-in-thick polyethylene; 8865K522, McMaster-Carr). To minimize thermal drift and the effects of air currents, we cover the entire apparatus in a foam-core box. We also allow all electronics associated with the microscope to warm up for a few hours before starting an experiment, so that any thermal gradients can equilibrate.

The coverslip and flow cells are mounted on a motorized three-axis stage (MAX343, Thorlabs) that has stepper motors for coarse adjustments and piezoelectric actuators for fine adjustments. The fine adjustments are used for active stabilization.

COVERSLIP FUNCTIONALIZATION

We treat the coverslips with (3-aminopropyl)triethoxysilane (APTES, 99%, Sigma-Aldrich) to impart a positive surface charge when the coverslips are submerged in neutral-pH buffer. The coverslips can then nonspecifically bind oppositely charged macroions such as nucleic acids and MS2 capsids, as shown in Extended Data Figure 3. Furthermore, the layer of amino groups can form covalent linkages through *N*-hydroxysuccinimide (NHS) chemistry. We form the PEG layer by adding 90- μL of 100 mM sodium bicarbonate buffer containing 9 mg of a 100:1 mixture of 5,000-Da NHS-PEG ($> 95\%$, Nanocs) and 5,000-Da NHS-PEG- N_3 (purity unreported, Nanocs)

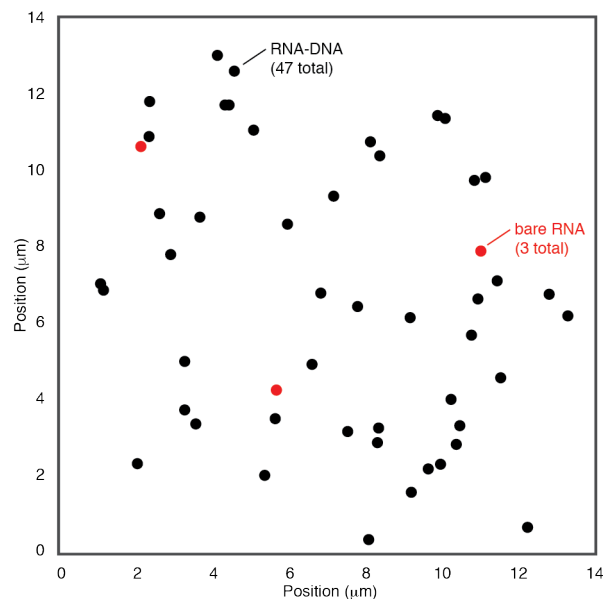
between two APTES-functionalized coverslips and then letting the ‘sandwich’ sit overnight at room temperature in a humid box before washing the slips with deionized water (obtained from a Millipore RNase-free system; Synthesis, Milli-Q). We attach DNA oligonucleotides to the surface-bound NHS-PEG-N₃ molecules by copper-free click chemistry. The 20-base-long oligonucleotides are synthesized with a dibenzocyclooctyne (DBCO) group on the 5’-end (RNase-free HPLC purified, Integrated DNA Technologies). We place 90 μ L of 10 μ M DBCO-DNA in phosphate-buffered saline (PBS without Ca or Mg, Lonza) between two coverslips and let the sandwich sit overnight at room temperature in a humid box. The sequence of the surface oligo is 5’-(DBCO)-GGTTGGTTGGTTGGTTGGTT-3’.

We test that the coverslips are functionalized with the surface oligo by measuring the specific binding of MS2 RNA that is hybridized to a complementary linker oligo using interferometric scattering microscopy (Supplementary Figure 2).

Following functionalization, we decorate the coverslips with 30-nm gold particles that serve as tracer particles for active stabilization. We purchase 30-nm amine-functionalized particles (Nanopartz) and conjugate them to NHS-PEG to prevent adsorption of coat proteins. The conjugation is done by adding 20 mg of NHS-PEG to 200 μ L of 10 nM of gold particles in 100 mM sodium bicarbonate buffer. The mixture is left overnight in a tube rotator. The particles are then washed five times by centrifuging the mixture at 8,000 g for 5 min and then resuspending in TE buffer (10 mM tris-HCl, pH 7.5; 1 mM EDTA). To allow the the PEG-passivated gold particles to bind non-specifically to the coverslip, we sandwich 70 μ L of 0.1 nM suspension of the particles between two coverslips and let them sit for 10 min at room temperature before washing the slips with deionized water. The method produces an average surface density of about 1 particle per 100 μ m², as measured in the interferometric scattering microscope. Functionalized coverslips are stored under nitrogen gas at -20° C and discarded after 2 months.

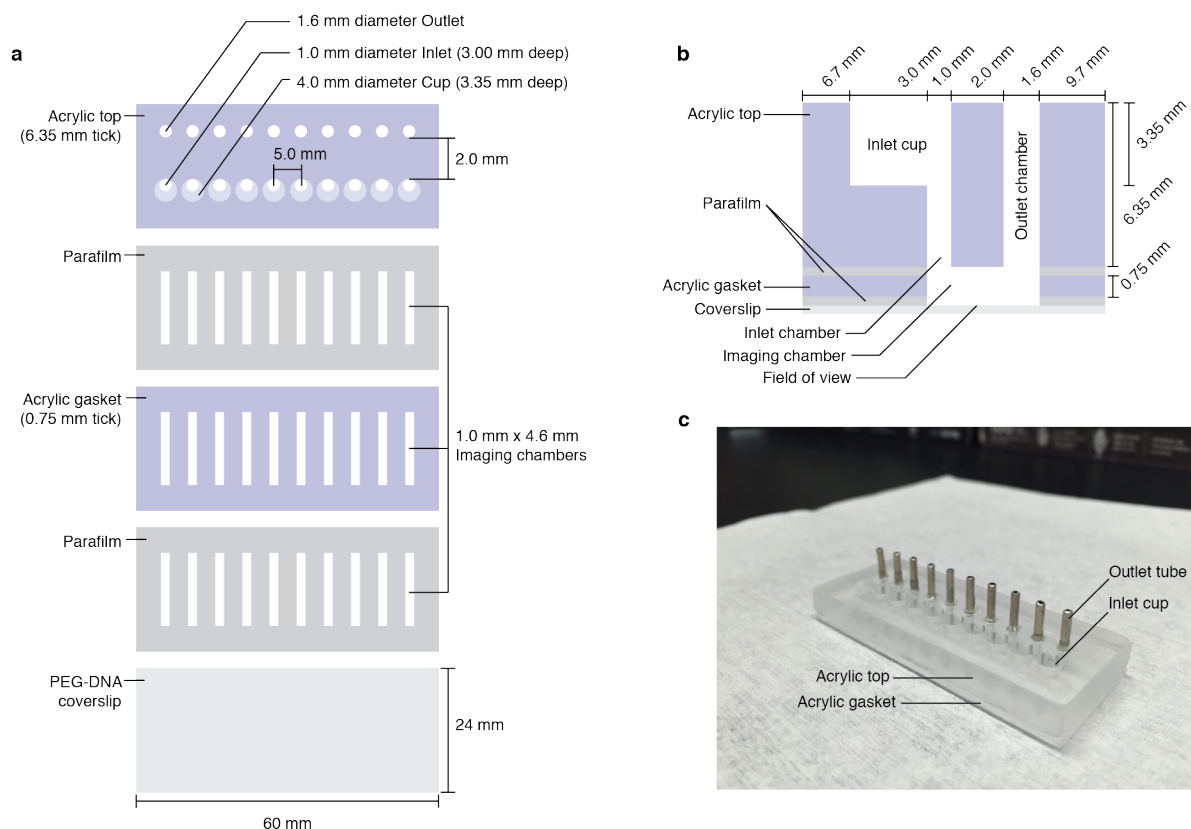
FLOW CELL DESIGN AND CONSTRUCTION

A schematic of each of the layers of the chip, a cross sectional view of a single flow cell, and a photograph of the final assembled state are shown in Supplementary Figure 3. The bottom acrylic sheet (Optix Acrylic, ePlastics) is 0.75 mm thick and contains 10 rectangular through-holes (1 mm \times 4.6 mm) that are cut with a laser cutter (HSE 150W, KERN). These rectangular holes form the imaging chamber of each flow cell. The top acrylic sheet (6.35 mm thick cast acrylic, McMaster-Carr) serves as the roof of the imaging chambers and contains the inlet cups, the inlet chambers, and the outlet chambers. Each inlet cup is 3.35 mm deep and 4 mm in diameter. Each inlet chamber is a 1-mm-diameter through-hole that begins at the base of an inlet cup and connects to an imaging chamber in the bottom acrylic sheet. The outlet chambers are 1.6-mm-diameter through-holes. We epoxy



SUPPLEMENTARY FIGURE 2. Specific binding of RNA to the coverslip via DNA linkages. To test whether the DNA-linkage enables specific binding of the RNA to the coverslip, solutions containing 1 nM of either bare RNA or RNA-DNA complexes in hybridization buffer are injected into the imaging chamber of the interferometric scattering microscope. If the binding is specific, we expect only the RNA-DNA complexes to stick to the coverslip surface. The bare RNA is injected first, and we image the system for 60 s to detect each molecule that binds. We then inject the RNA-DNA complexes, and we repeat the measurement. The location of each detected binding event is shown: we observe a total of 3 bare RNA molecules (red circles) and 47 RNA-DNA complexes (black circles). We conclude that the binding between the RNA-DNA complexes and the coverslip is highly specific, and that most of the RNA-DNA complexes that are bound to the coverslip are tethered by a DNA linkage.

(5 minute epoxy, Devcon) a 10-mm-long aluminum tube (inner diameter 0.9 mm, outer diameter 1.6 mm, McMaster-Carr) into each outlet chamber. All holes in the top acrylic piece are machined with a mill. The Parafilm sheets used to seal together the layers of the flow cell contain rectangular gaps that are the same size as the imaging chambers. The gaps are cut with a computer-controlled vinyl cutter (CAMM-1 Servo, Roland).



SUPPLEMENTARY FIGURE 3. A schematic of the rigid flow cell. (a) Each of the layers used to build the flow cell are stacked on top of one another. When heated, the Parafilm seals the layers together. (b) A cross-section of a flow cell. (c) A photo of an assembled flow cell. Aluminum tubes are epoxied into the outlet chambers to connect to the Tygon tubing.

To assemble each chip, we first clean the acrylic sheets and Parafilm by sonicating in a 2% w/v aqueous solution of sodium dodecyl sulfate (>99%, Sigma-Aldrich) for 30 min. After sonicating, we rinse the acrylic and Parafilm with deionized water and then dry them under a stream of nitrogen gas. Next, we press one sheet of Parafilm onto the bottom acrylic sheet so that the Parafilm and acrylic stick together, and we place this assembly in a 65 °C oven for 5 min. The top acrylic sheet is also placed in the oven for 5 min. When we remove the acrylic sheets from the oven and press them firmly together, the melted Parafilm seals the two sheets of acrylic together to form the chip. We then press the other sheet of Parafilm onto the bottom of the chip so that it sticks, and we place the chip in a 65 °C oven for 5 min. We remove the chip from the oven and press it firmly onto the functionalized

coverslip (which is not heated) to seal the chip to the coverslip. We use all of the flow cells on a coverslip within one or two days.

We inject buffer solution into each imaging chamber using a plastic syringe (3 mL BD, VWR) that is connected to the aluminum outlet tube by a short (approximately 4 cm) length of tubing (Tygon PVC, McMaster-Carr). We fill the inlet cup with solution and then pull it through the imaging chamber by actuating the syringe with a motorized linear translation stage (PT1-Z8, Thorlabs). Each time we inject a solution into the imaging chamber, we use the motorized stage to inject 10 μL of solution at a constant rate over 20 s. Before further injections we use a Kimwipe (Kimberly-Clark Professional) to wick any remaining solution from the inlet cup. To ensure that the fluid injection is reproducible, we prevent any air bubbles from entering the flow cell, tubing, or syringe. We mount the syringe vertically to prevent air bubbles from being trapped inside it.

ASSESSING THE CONCENTRATION AND PURITY OF MS2 VIRUS PARTICLES, AND OF ISOLATED COAT PROTEIN AND RNA

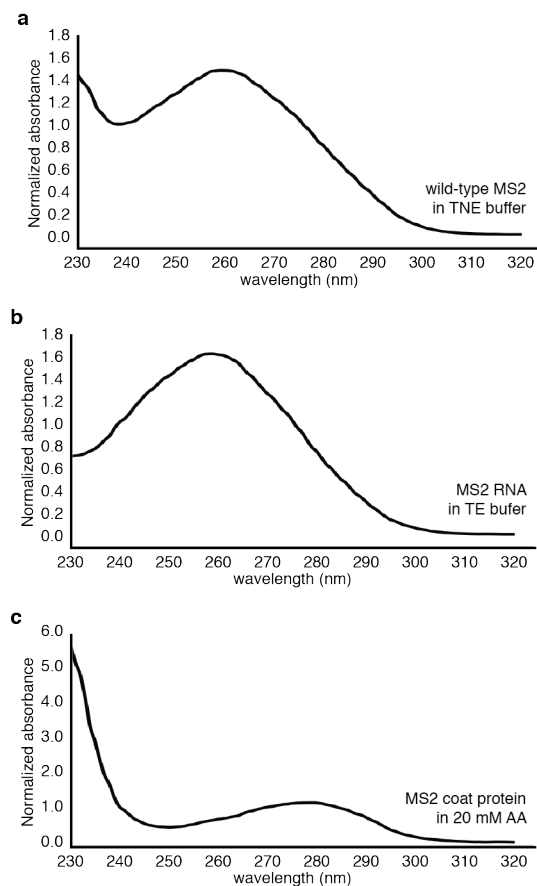
We determine the concentration of MS2 by UV-spectrophotometry (NanoDrop-1000, Thermo Scientific), assuming an extinction coefficient of 8.03 $\text{mL mg}^{-1} \text{cm}^{-1}$ at 260 nm (Ref. 3).

After purifying the coat protein from wild-type virus particles using cold acetic acid, we exchange the coat-protein buffer for 20 mM acetic acid using 3-kDa-MWCO centrifugal filter units (EMD Millipore). In 20 mM acetic acid, the coat proteins form non-covalent dimers. We determine the concentration of coat-protein dimers by UV-spectrophotometry, using an extinction coefficient of 33200 $\text{M}^{-1} \text{cm}^{-1}$ at 280 nm (Ref. 2). We check for RNA contamination by measuring the ratio of the UV-absorbance at 260 nm to that at 280 nm (Supplementary Figure 4). We use only protein that has a 260/280 ratio less than 0.67 for assembly.

After purifying the RNA from wild-type virus particles using an RNeasy kit, we collect the RNA in TE buffer (10 mM Tris-HCl, pH 7.5; 1 mM EDTA) and determine its concentration by UV-spectrophotometry using an extinction coefficient of 0.025 $\text{mL mg}^{-1} \text{cm}^{-1}$ at 260 nm. We check for protein contamination by measuring the ratio of the UV-absorbance at 260 nm to that at 280 nm (Supplementary Figure 4). We use only RNA that has a 260/280 ratio greater than 2.0 for assembly. Then we check the integrity of the RNA by native 1% agarose gel electrophoresis (Supplementary Figure 5).

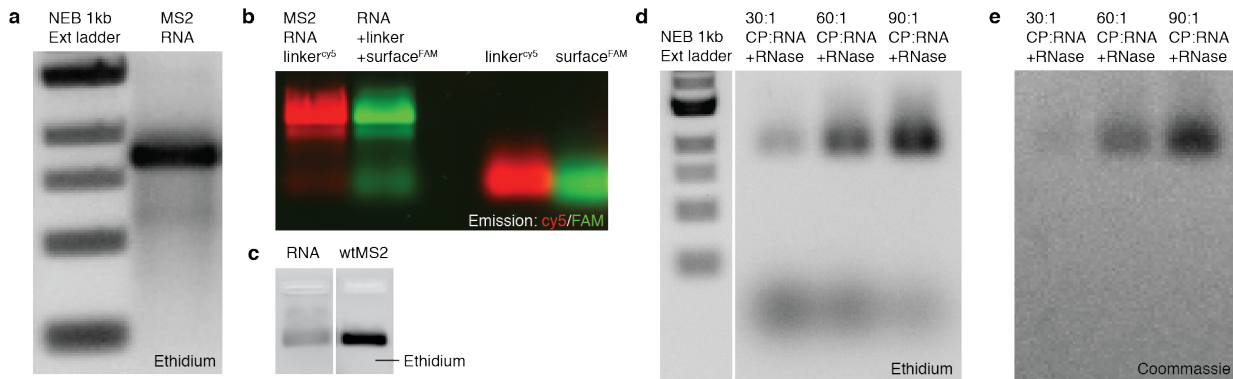
CRITERIA FOR REJECTING SPOTS FOR ANALYSIS

The spots from particles that adsorb to the coverslip are easily identified because they appear instantaneously in one frame of the movie instead of gradually appearing over the course of many frames. In some cases, such particles can be seen approaching the coverslip before adsorption.



SUPPLEMENTARY FIGURE 4. Purities of wild-type MS2 virus, its RNA, and its coat protein are determined by UV-vis spectrophotometry. Absorbance spectra for purified (a) wild-type MS2, (b) MS2 RNA, and (c) MS2 coat protein. The 260/280 ratio of wild-type MS2 in TNE buffer is 1.84, of MS2 RNA in TE buffer is 2.16, and of unassembled coat-protein dimers in 20 mM acetic acid is 0.58. Each spectrum is normalized so that the absorbance is 1.0 at 240 nm. All absorbance measurements are made using a Nanodrop-1000 spectrophotometer (Thermo Scientific).

Spots within 8 pixels of the gold particle used for active stabilization or a bright defect on the coverslip are rejected. There are typically fewer than 2 defects on the coverslip in a given field of view. The spots that grow near the gold particle or defect are not analyzed because they may be due to growth that occurs on the gold particle or defect instead of on the RNA.



SUPPLEMENTARY FIGURE 5. Native agarose gel electrophoresis is used to determine the integrity of the RNA, the yield of RNA-DNA hybridization, and the yield of RNA packaging by MS2 coat protein. All gels consist of 1% agarose in TAE buffer. (a) The MS2 RNA used in the assembly experiments appears as a single band with minimal smearing, indicating that the RNA is not degraded. The left lane contains a 1-kb extended DNA ladder (New England Biolabs), and the right lane contains 1 μ g of MS2 RNA. The gel is visualized after staining with Gel Red (Biotium Inc.) ethidium stain. (b) Fluorescent linker and surface oligos migrate with the RNA after hybridization and purification, indicating strong specific binding. The leftmost lane is prepared by mixing 1 μ g of MS2 RNA and a 10-fold molar excess of fluorescently labeled (5'-cy5) linker oligo (Integrated DNA Technologies). The RNA is hybridized to the linker by thermal annealing, and the unbound linker is removed by centrifugal filtration. The second-to-leftmost lane is prepared by mixing 1 μ g of MS2 RNA and a 10-fold molar excess of non-fluorescent linker oligo. The RNA and linker oligo are hybridized and the unbound linker purified as before. Then a stoichiometric amount of fluorescently labeled (5'-FAM) surface oligo (Integrated DNA Technologies) is added. The second-to-rightmost lane contains free 5'-cy5 linker oligo, and the rightmost contains free 5'-FAM surface oligo. The gel is visualized without staining by imaging the fluorescence emission of the cy5 and FAM dyes on separate channels. (c) MS2 RNA and wild-type virus particles migrate to the same position in the gel. The left lane contains RNA, and the right lane contains virus particles. The gel is visualized after staining with ethidium. (d) MS2 coat-protein dimers (CP) package MS2 RNA into RNase protected complexes with the same mobility as wild-type virus particles. The leftmost lane contains 1-kb extended ladder. The next three lanes are prepared by mixing 1 μ g of MS2 RNA and increasing molar ratios of CP in 10 μ L of TNE buffer. The mixtures are incubated for 30 min at room temperature and then treated with 10 ng of RNase A (Amresco Inc.). Electrophoresis is performed 30 min after RNase treatment, and the gel is visualized after staining with ethidium. Protected RNA migrates with the same mobility as wild-type virus particles, and digested RNA migrates farther down the gel. The amount of digested RNA decreases with increasing CP. (e) Assembling particles prepared and then treated with RNase as just described contain protein, as evidenced by staining with coomassie (Instant Blue) protein stain.

Furthermore, the in-plane active stabilization keeps the coverslip position constant to within only a few nanometers, and when particles as bright as the gold particles move by a few nanometers they produce intensity changes that are similar to or larger than the intensity of an MS2 capsid. These intensity changes affect the measured intensity of any nearby assembling particles.

To determine if a spot is near a particle that adsorbs to or desorbs from the coverslip, we check if the interference fringes of an absorbing or desorbing particle overlap with the spot at any point during the movie. If they do, we examine the intensity of the particle as a function of time to check if there is an abrupt change in intensity that occurs on the same frame as the adsorption or desorption event. If the abrupt change in intensity is greater than 0.0003 (10% of the intensity of a capsid), we reject the spot for analysis. By not analyzing these spots, we avoid misinterpreting intensity changes that are due to the adsorption or desorption event as features of the assembly kinetics.

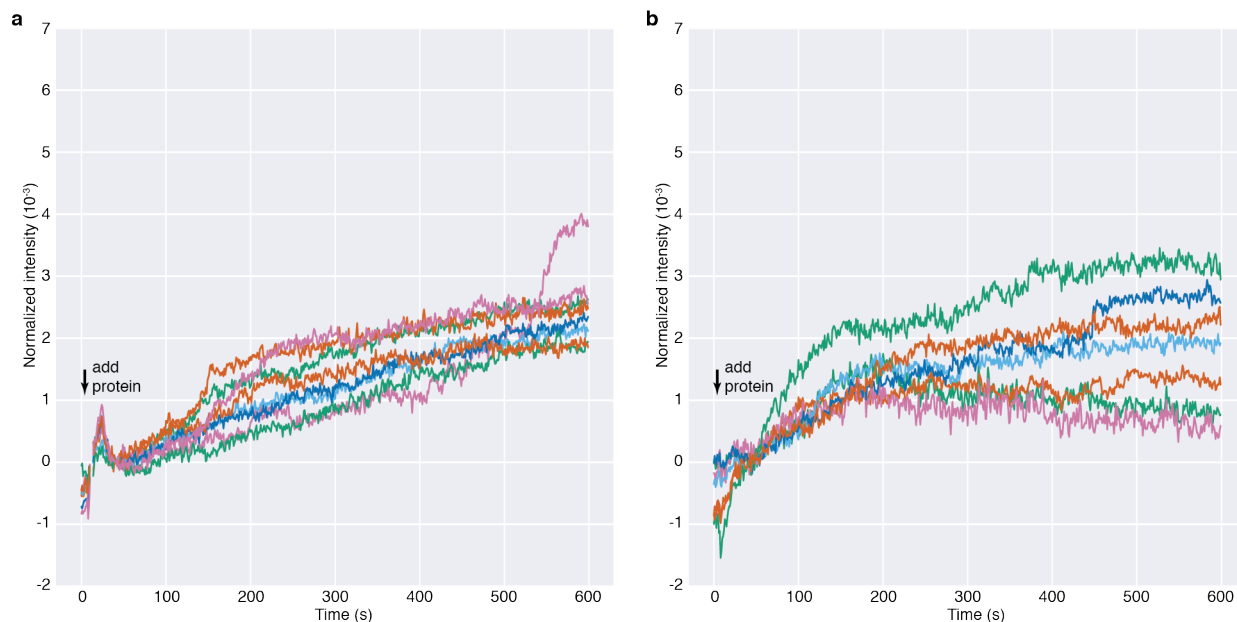
A spot is determined to be too close to another spot if their centers are within 4 pixels of each other. If two spots are closer than this distance, their interference fringes overlap, and the measured intensity of each will depend on the intensity of the other.

Similarly, we do not analyze any spot with a center that is within 4 pixels of the edge of the field of view. We do not analyze these spots because the interference patterns for the spot are not fully visible, and we cannot determine if there are particles beyond the edge of the field of view that affect the spot's intensity.

Finally, we do not analyze spots that grow slowly and synchronously with a consistent growth rate over the course of the measurement (Supplementary Figure 6). In a typical experiment, we observe 1–10 of these spots (Supplementary Movie 1). We observe a similar number of spots with similar growth kinetics in control experiments where RNA is not added to the surface (Supplementary Movie 5). We therefore conclude that these spots likely do *not* represent the assembly of coat-protein dimers around RNA. They may represent protein aggregates growing on the coverslip surface.

CONTROL ASSEMBLY EXPERIMENTS AT LOWER ILLUMINATION INTENSITY

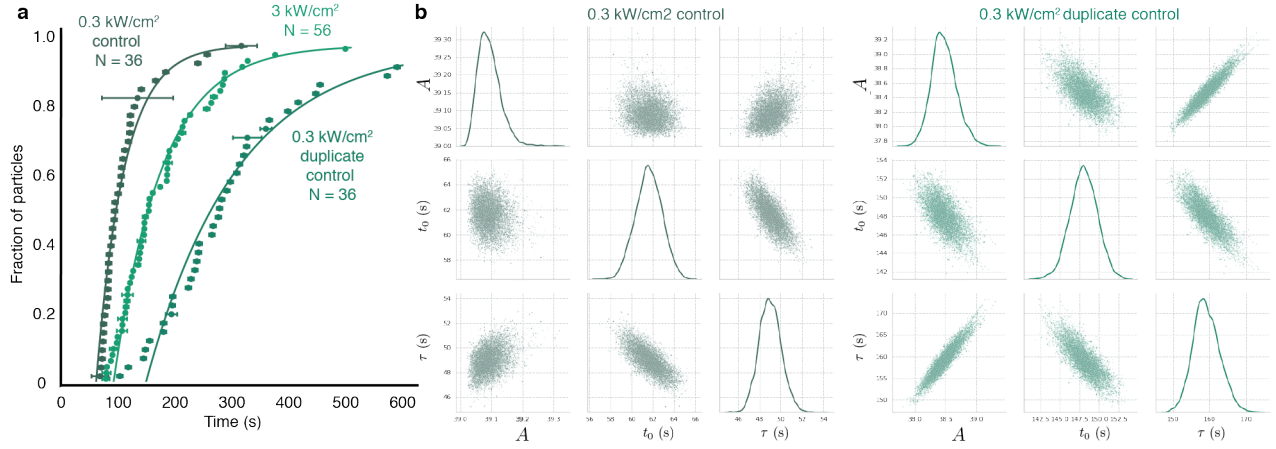
The results of control experiments at lower illumination intensity and 2 μ M protein shown in Supplementary Figure 7 are similar to those of the higher-intensity experiment presented in Figure 2 of the main text and Extended Data Figures 2 and 5. Again, different assembling particles appear after different start times. The cumulative distribution function of the start times is well-fit by the same exponential function but with $t_0 = 62 \pm 1$ s, $A = 39.08^{+0.04}_{-0.03}$, and $\tau = 49 \pm 1$ s for the first control experiment of the duplicate set, and $t_0 = 148 \pm 2$ s, $A = 38.5 \pm 0.2$, and $\tau = 159 \pm 4$ s for the second control experiment. 24 out of 39 traces plateau at intensities



SUPPLEMENTARY FIGURE 6. Some of the spots that appear in assembly experiments do not represent assembly around RNA. (a) In the assembly experiment from the main text where we use $2\ \mu\text{M}$ coat-protein dimers, we observe 8 spots (in addition to the 56 assembling particles described in the text) that grow slowly and synchronously and that show a consistent growth rate over the course of the measurement. The traces of these particles are shown in the plot, which is a 1,000-frame average of the intensities measured from Supplementary Movie 1, recorded at 1,000 Hz. (b) In a control experiment with $2\ \mu\text{M}$ dimers but no RNA on the surface, we observe 7 spots that grow slowly and synchronously, with traces similar to those shown in panel (a). For this experiment, we bound the linker oligos to the surface oligos, but we did not add the RNA. The traces are measured from the data in Supplementary Movie 5. The data is recorded at 1,000 Hz and is plotted with a 1,000-frame average.

consistent with that of a full capsid, 2 plateau at smaller intensities, and 13 plateau at larger intensities in the first control experiment, while 25 out of 36 traces plateau at intensities consistent with that of a full capsid, 5 plateau at smaller intensities, and 6 plateau at larger intensities in the second experiment. These fractions are similar to those observed in the $2\ \mu\text{M}$ experiment presented in the main text.

The results of the control experiments indicate that the incident light does not qualitatively affect the assembly process. The observed kinetic traces and distribution of start times are consistent with those expected from a nucleation-and-growth process. Moreover, because the difference between identically performed low-intensity control experiments is larger than those



SUPPLEMENTARY FIGURE 7. Comparison of the nucleation kinetics for independent assembly experiments performed with 2 μM of coat-protein dimers. (a) To test if the intensity of the illumination beam affects the assembly process, we compare the cumulative distribution of start times for the experiment described in Figure 2 to that of a set of duplicate control experiments, where the illumination intensity is an order of magnitude smaller. The difference in the characteristic times for the duplicate control experiments is larger than the difference between the higher illumination intensity experiments and either of the controls, suggesting that other experimental uncertainties, such as differences in the injected protein concentration or in the flow profile within the imaging chamber, have a larger effect on the kinetics than the illumination intensity. The error bars represent the uncertainty in the time measurement, as described in the Methods. (b) The posterior probability distributions of parameter values obtained by fitting the data from the control experiments. The plots along the diagonal show kernel density estimates of the fully marginalized posterior distributions of each parameter, while the off-diagonal plots show the joint distributions.

between the high-intensity experiments and either of the controls, we conclude that other factors, such as differences in the concentration of protein, are responsible for the variation. Indeed, the variation in both the fitted time constants, τ , and the delay times, t_0 among different experiments is not unexpected, given the strong dependence of the start times on concentration. At 1 μM protein concentration, all the start times are longer than the 600-s duration of the experiment, so that even a slight difference in the protein concentration introduced during the 2 μM experiments could cause the 110-s spread between the measured time constants and the 86-s spread in the delay times.

SUPPLEMENTARY MOVIES

Supplementary Movie 1: The time-series of images from the assembly experiment using 2 μM protein (Figs. 1, 2, and 3, Extended Data Fig. 2, and Supplementary Figs. 6 and 7). The time-series is recorded at 1,000 Hz, is shown with a 1,000-frame average, and is sped up by a factor of 100 for playback. The field of view is 9.8 μm on each side.

Supplementary Movie 2: The time-series of images from the assembly experiment using 1 μM protein (Extended Data Fig. 6). The time-series is recorded at 100 Hz, is shown with a 300-frame average, and is sped up by a factor of 200 for playback. The field of view is 14 μm on each side. The illumination beam is blocked for a short time approximately halfway through the movie, just before 2 μM protein is added. In the first half of the movie, where 1 μM protein is in the imaging chamber, a few particles are seen adsorbing to the coverslip, but no particles are seen growing on the coverslip. In the second half of the movie, where 2 μM of protein is in the imaging chamber, a number of particles are seen growing on the coverslip.

Supplementary Movie 3: The time-series of images from the assembly experiment using 1.5 μM protein (Fig. 3, Extended Data Fig. 7). The time-series is recorded at 1,000 Hz, is shown with a 1,000-frame average, and is sped up by a factor of 100 for playback. The field of view is 9.8 μm on each side.

Supplementary Movie 4: The time-series of images from the assembly experiment using 4 μM protein (Fig. 3, Extended Data Fig. 8). The time-series is recorded at 1,000 Hz, is shown with a 1,000-frame average, and is sped up by a factor of 100 for playback. The field of view is 9.8 μm on each side.

Supplementary Movie 5: The time-series of images from the control experiment using 2 μM protein with no RNA on the coverslip (Supplementary Fig. 6). The time-series is recorded at 1,000 Hz, is shown with a 1,000-frame average, and is sped up by a factor of 100 for playback. The field of view is 9.8 μm on each side.

REFERENCES

- [1] Happel, J.; Brenner, H. *Low Reynolds number hydrodynamics: with special applications to particulate media*; Springer Science & Business Media, 2012; Vol. 1.
- [2] Borodavka, A.; Tuma, R.; Stockley, P. G. *Proceedings of the National Academy of Sciences* **2012**, *109*, 15769–15774.

- [3] Strauss, J. H.; Sinsheimer, R. L. *Journal of Molecular Biology* **1963**, *7*, 43 – 54.